Spring 2018

Investigation of microstructure and mechanical properties by direct metal deposition

Jingwei Zhang

Department: Mechanical and Aerospace Engineering

INVESTIGATION OF MICROSTRUCTURE AND MECHANICAL PROPERTIES BY DIRECT METAL DEPOSITION

by

JINGWEI ZHANG

A DISSERTATION

Presented to the Graduate Faculty of the

MISSOURI UNIVERSITY OF SCIENCE AND TECHNOLOGY

In Partial Fulfillment of the Requirements for the Degree

DOCTOR OF PHILOSOPHY

in

MECHANICAL ENGINEERING

2018

Approved by

Dr. Frank Liou, Advisor
Dr. Kelly Homan
Dr. Joseph Newkirk
Dr. K. Chandrashekhara
Dr. Heng Pan

PUBLICATION DISSERTATION OPTION

This dissertation consists of the following three articles which have been submitted for publication, or will be submitted for publication as follows:

Paper I: Pages 6-27 have been published by Additive Manufacturing Journal.

Paper II: Pages 28-55 have been accepted by the chapter for the book Three-dimensional Printing and Additive Manufacturing of High-performance Metals and Alloys.

Paper III: Pages 56-79 have been accepted by Rapid Prototyping Journal.

ABSTRACT

Microstructure and properties of Direct Metal Deposition (DMD) parts are very crucial to meeting industrial requirements of parts quality. Prediction, and control of microstructure and mechanical properties have attracted much attention during conventional metal manufacturing process under different conditions. However, there is few investigations focused on microstructure simulation and mechanical properties control under different process parameters during DMD process. This dissertation is intended to develop a multi-scale model to investigate Ti6Al4V grain structure development and explore Ti6Al4V based functionally graded material (FGM) deposit properties during DMD process. The first research topic is to investigate and develop a cellular automaton-finite element (CA-FE) coupled model to combine with thermal history and simulate nucleation sites, grain growth orientation and rate, epitaxial growth of new grains, remelting of preexisting grains, metal addition, and grain competitive growth. The second research topic is to develop grain growth algorithm, which is appropriate for highly non-uniform temperature field and high cooling rate, to control grain structure under real-time changing process parameters. The third research topic is to investigate the influence of process parameters on microstructure and properties of Ti6Al4V-based FGMs, which are fabricated with different TiC volume fraction from 0 to 30vol%. The microstructure, Vickers hardness, phase identification, tensile properties of FGM are measured to investigate the fabricated FGM qualities. The Digital Image Correlation (DIC) is developed to analyze Young's modulus versus composition of FGM parts.

ACKNOWLEDGMENTS

First and foremost, I would like to express my sincere gratitude to my advisor, Dr. Frank Liou, for his encouragement, insightful guidance, and support during my Ph.D. study at Missouri University of Science and Technology. His diligence and rigorous altitude to research and work will have a significant influence on my life. It has been a privilege and a great honor to have worked with him.

I would also like to extend my appreciation to all my dissertation committee members, Dr. Joseph Newkirk, Dr. K. Chandrashekhara, Dr. Heng Pan, and Dr. Kelly Homan. Without their patient guidance and valuable comments, it would have been impossible for me to complete my dissertation. This dissertation was supported by the Laser Aided Manufacturing Processes (LAMP) Laboratory, and NASA Langley Research Center, which are gratefully acknowledged.

I would like to express my deep thanks to my lab-mates and friends, Mr. Wei Li, Mr. Sreekar Karnati, Mr. Yunlu Zhang, Mr. Lei Yan, Mr. Renwei Liu, Mr. Zhiyuan Wang, Mr. Arron Flood, Ms. Xueyang Chen, Mr. Xinchang Zhang, and Ms. Wenyuan Cui for their support during my phD study in Rolla.

Last but not the least, I wish to extend my special and sincere thanks to my parents, Mr. Jianping Zhang and Ms. Shuqing Wang, my fiancee, Junqi Liu, and all my family members for their love and unwavering support.

TABLE OF CONTENTS

Page

LIST OF ILLUSTRATIONS

PAPER III

LIST OF TABLES

SECTION

1. INTRODUCTION

1.1. BACKGROUND

Compared with the conventional subtractive manufacturing technologies, additive manufacturing (AM) has unique advantages including low heat input, small heat-affected zone, solid-free-form fabrication, near-net-shape, low material waste, and so on. Direct metal deposition (DMD), a rapid developing AM technique, is able to manufacture a fully dense metal part without intermediate steps, which is especially appropriate for the heterogeneous components manufacturing. The microstructure evolution during manufacturing process is definitely different from conventional casting and welding since it is under higher cooling rate, highly non-equilibrium condition, cycling heating and cooling process and real-time material addition. The as-deposit microstructure plays a critical role in determining parts'mechanical properties, which is directly affected by material itself and the whole manufacturing process. Therefore, the prediction and control of microstructure and properties during DMD are necessary such that as-deposit metal parts can meet strict industrial requirements.

DMD is especially appropriate for manufacturing heterogeneous parts because it can change feeding material composition, thus changing parts'microstructure, and properties smoothly. The advantages of multiple materials can be obtained within one part, which extend the application situation of as-deposit parts. Titanium alloys, especially the Ti6Al4V alloy, are widely utilized in aerospace industry, medical apparatus and manufacturing application. The reason is that Ti6Al4V possesses excellent properties, which includes high-strength-to-weight ratio, high temperature strength, low density and excellent

corrosion resistance. However, Ti6Al4V doesn't have high surface hardness, stiffness or wear resistance, which limits Ti6Al4V application in some extreme conditions. Conventional composite, such as Matrix Metal Composite (MMC), can improve parts' performance to some extent. However, the material ratio and selection are limited very much since different Coefficient of Thermal Expansion (CTE) among different materials can result in crack readily when the ratio is high. Functionally gradient materials (FGM) with DMD technique can be selected as a potential to both improve material properties and build crack and pore free deposited parts. A series of process parameters and material composition will prominently influence the parts' qualities and microstructure, which determine the thermos-physical and mechanical properties. This dissertation investigates microstructure prediction of as-deposit parts, the effect of process parameters and TiC composition on microstructure, hardness and mechanical properties of FGM parts.

1.2. RESEARCH OBJECTIVES

The main objective of this dissertation is to develop a multi-scale model to investigate Ti6Al4V grain structure development and explore Ti6Al4V based FGM deposit parts microstructure and properties during DMD process.

The objective of the research task one is to predict microstructure evolution of single-layer and multiple-layer part during DMD process. Actually, there are two sub-tasks for research task one. The first one is to calculate the temperature field of the whole part, which offers the thermal history of macroscopic nodes and are validated by the experiment. The second one is to develop a multi-scale predictive model to simulate nucleation sites, grain growth orientation selection and growth rate, epitaxial growth of new grains on the interface, remelting of preexisting grains, metal addition, grain competitive growth, and columnar to equiaxed transition phenomenon within substrate and melt pool domain.

Based on the predictive multiscale model, a 2D single-layer and multiple-layer simulation is conducted to provide a guideline of microstructure evolution. The predictive simulation is also validated by the DMD experiment with Ti6Al4V material.

The second task is to develop CA grain growth algorithm, which is appropriate for highly non-uniform temperature field and high cooling rate, to control grain structure. A "decentered polygon"algorithm is proposed to solve grain growth under non-equilibrium condition during AM manufacturing process. Compared to conventional grain growth algorithm, the simulation result of new algorithm is more closed to experimental result. The grains keep the original orientation, and the overgrowth effect among grains can be achieved, which is agreement well with experiment. The third research task is to investigate the effect of process parameters and TiC composition on microstructure, hardness and mechanical properties of as-deposit FGM parts. The effect of laser power, scan speed, and material composition on microstructure and Vickers hardness are investigated. The relationship between energy density and dendritic arm spacing is evaluated. Current work presents unique and original contributions from the study of miniature FGM tensile specimens using DIC method. It investigates the effect of specimen orientation and TiC content on Young's modulus and UTS.

The outcomes of the above research tasks are expected to lead to new knowledge that simulates the grain structure development of single-layer and multiple-layer deposition and improves microstructure, hardness, and stiffness of Titanium alloy for structural application during DMD process. The boarder impact is considerable. The model can be applied in large-scale thermal and microstructural evolution, including millions of grains. The process parameters can be optimized to control microstructure, thus obtain admired microstructure and properties. Some properties, such as Young's modulus, can also be the reference for some modeling computation of FGM.

1.3. ORGANIZATION OF DISSERTATION

In this dissertation, three major research and developments are presented and organized as shown in Figure 1.1. Paper I focuses on building a predictive model based on a cellular automaton (CA)-finite element (FE) method to simulate thermal history and microstructure evolution during metal solidification for DMD process. The macroscopic FE calculation was designed to update the temperature field and simulate a high cooling rate. In the mesoscopic CA model, heterogeneous nucleation sites, preferential growth orientation, and grain growth rate were simulated. The CA model is able to show the entrapment of neighboring cells and the relationship between undercooling and the grain growth rate. The model predicted the grain size, orientation, and morphological evolution during the solidification phase of the deposition process. Paper II aims to develop grain growth algorithm, which is appropriate for highly non-uniform temperature field and high cooling rate, to control grain structure. By comparing to previous growth method, it is proved that the developed "Decentred Polygon"growth method can keep grain orientation and simulate grain overgrowth mechanism, which is closer to experimental observation. Paper III investigates the effect of process parameters and composition on microstructure and properties of Ti6Al4V-based FGMs, which are fabricated with different TiC volume fraction from 0 to 30vol%. The microstructure, Vickers hardness, Young's modulus, and UTS of FGM are measured and analyzed under different laser power and scan speed.

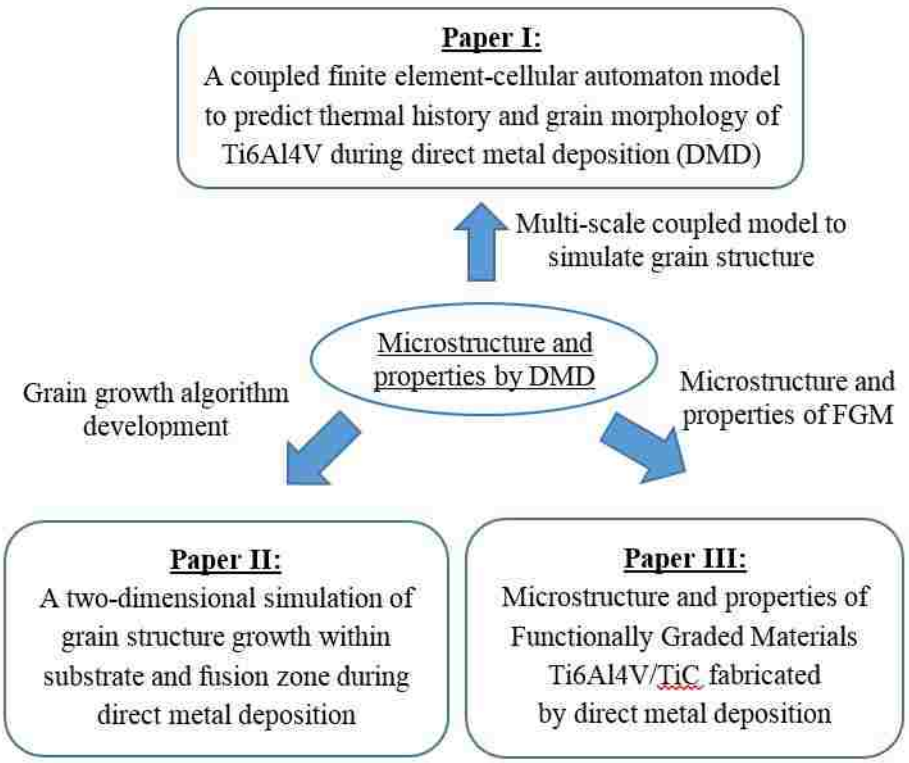

Figure 1.1. Framework of this dissertation

PAPER

I. A COUPLED FINITE ELEMENT CELLULAR AUTOMATON MODEL TO PREDICT THERMAL HISTORY AND GRAIN MORPHOLOGY OF TI6AL4V DURING DIRECT METALDEPOSITION (DMD)

Jingwei Zhang[a], Frank Liou[a], William Seufzer[b], Karen Taminger[b]

[a]Department of Mechanical & Aerospace Engineering

Missouri University of Science and Technology

Rolla, Missouri 65409–0050

[b]Langley Research Center, National Aeronautics and Space Administration

Hampton, VA 23681, United States

ABSTRACT

In this paper, a predictive model based on a cellular automaton (CA)-finite element (FE) method has been developed to simulate thermal history and microstructure evolution during metal solidification for the laser-based additive manufacturing process. The macroscopic FE calculation was designed to update the temperature field and simulate a high cooling rate. In the microscopic CA model, heterogeneous nucleation sites, preferential growth orientation, and dendritic grain growth were simulated. The CA model was able to show the entrapment of neighboring cells and the relationship between undercooling and the grain growth rate. The model predicted the dendritic grain size, and morphological evolution during the solidification phase of the deposition process. The grain morphology result has been validated by the experiment.

Keywords: Heat transfer, Finite element analysis, Cellular automaton, Grain growth, Direct metal deposition

1. INTRODUCTION

Additive Manufacturing (AM) technology is used to produce physical models, prototypes, or functional gradient components directly from 3D computer-aided design (CAD) data. The thermal history of the whole component and the microstructure after solidification play a critical role in the metallurgical and mechanical properties, which are the main concerns for engineers. As shown in Figure 1, the laser deposition system uses a focused laser heat source to generate a molten pool on a substrate and melt injected powder, thus creating a fully dense deposited bead. Ehsan Toyserkani et al. [1] developed a 3D transient finite element model of laser cladding by powder injection to research the effects of laser pulse shaping on the process. Masoud Alimardani et al. [2] presented a 3D transient numerical approach for modeling the multilayer laser solid freeform fabrication (LSFF) process to predict time dependent geometry, temperature, and thermal stress fields, which was verified by the AISI 304L stainless steel experiment. Solidification thermal history affects microstructure evolution, which directly affects materials'mechanical properties. Several approaches have been taken to model microstructure evolution. A Monte Carlo stochastic method was shown by M. Anderson et al. [3], but this method does not explicitly consider the relationship between the growth rate of dendrite tips and undercooling. A phase field method was used by Choudhury et al. [4], but this method carried a high computational cost because of a requirement for a very fine computational grid. Another method employs a cellular automaton (CA) method proposed by Rappaz and Gandin [5]. The CA algorithm characterizes the discrete temporal and spatial microstructural evolution by utilizing a network of regular cells [6].The advantages of the CA model are that it is based on a strict physical mechanism and has a low computation cost. The CA model can be coupled with a macroscopic thermal model to consider heat and mass transfer in complex geometries. The CA method for prediction of microstructure development was used to simulate the microstructure. Gandin et al. [7][8] developed a 2D and 3D cellular automaton (CA)-finite element (FE) model for the prediction of solidification grain structures. Gildas Guille-

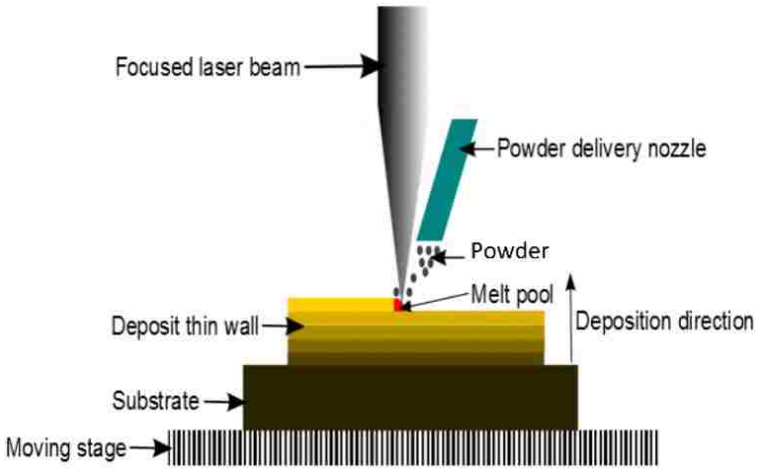

Figure 1. Laser deposition system schematic

mot et al. [9] investigated the prediction of solidification grain structures coupled with the calculation of solid and liquid flow induced macrosegregation with a coupled FE-CA mode. Zhijian Wang et al. [10] utilized FE-CA method to simulate the TC4 titanium alloy grain structure of molten pool during laser cladding solidification. However, there is little investigation on predicting one-layer and multiple-layer Ti-6Al-4V grain morphology and obtaining experimental validation during direct metal deposition (DMD).

In this study, ABAQUS was used to calculate the temperature field of the whole part, which offers the macroscopic FE nodes'temperature. Interpolation was utilized to obtain the finer nodes'temperature based on the FE nodes result. The CA model was built to simulate the microstructure information, such as the dendritic grain size and columnar grain orientation. The microstructure simulation results were validated by the experiment. The model parameters for the simulations were based on Ti-6Al-4V material.

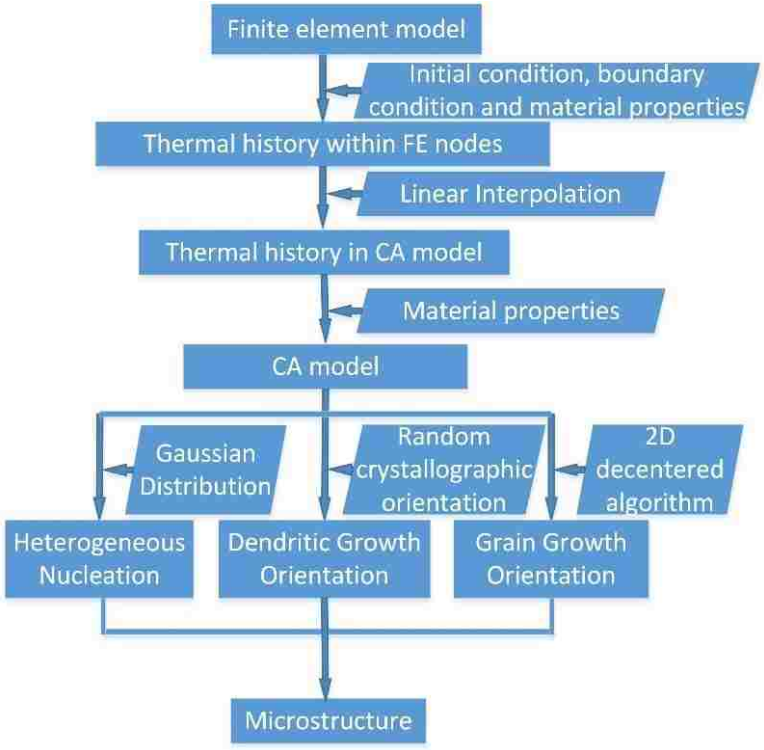

Figure 2. Flow chart of coupling FE-CA model

2. MATHEMATICAL MODEL

2.1. FINITE ELEMENT MODEL OF THERMAL ANALYSIS DURING LASER METAL DEPOSITION (LMD)

2.1.1. Governing Equations in Heat Transfer. In the laser metal deposition (LMD) process, the temperature history of the whole domain directly influences the deposition microstructure, which is critical to mechanical properties [11]. In order to obtain the microstructure information during the solidification process, the temperature field must be known at each time step. The transient temperature field throughout the domain was obtained by solving the 3D heat conduction equation (1), in the substrate, along with the appropriate initial and boundary conditions [12].

$$\rho(T) \cdot c_p(T) \cdot \frac{\partial T}{\partial t} = \frac{\partial}{\partial x}\left(k(T)\frac{\partial T}{\partial x}\right) + \frac{\partial}{\partial y}\left(k(T)\frac{\partial T}{\partial y}\right) + \frac{\partial}{\partial z}\left(k(T)\frac{\partial T}{\partial z}\right) + \dot{Q} \qquad (1)$$

where T is the temperature, $\rho(T)$ is the density, $c_p(T)$ is the specific heat, $k(T)$ is the heat conductivity, and $\dot{Q}$ is the internal heat generation following certain energy distribution per unit volume.

2.1.2. Initial Conditions and Boundary Conditions. The initial conditions applied to solve (1) were:

$$T(x, y, z, 0) = T_0 \tag{2a}$$

$$T(x, y, z, \infty) = T_0 \tag{2b}$$

where T_0 is the ambient temperature. In this study, T_0 was set as room temperature, 298 K. The boundary conditions, including thermal convection and radiation, are described by Newton's law of cooling and the Stefan-Boltzmann law, respectively. The laser heating source term $\dot{Q}$, in (1), also was considered in the boundary conditions as a surface heat source. The boundary conditions then could be expressed as [12]

$$K(\Delta T \cdot n)\,|_{\Gamma} = \left[-h(T - T_0) - \varepsilon(T)\,\sigma\left(T_0^4 - T_0\right)\right]\,|_{\Gamma}, \Gamma \notin \Lambda \tag{3a}$$

$$K(\Delta T \cdot n)\,|_{\Gamma} = \left[Q - h(T - T_0) - \varepsilon(T)\,\sigma\left(T_0^4 - T_0\right)\right]\,|_{\Gamma}, \Gamma \in \Lambda \tag{3b}$$

where k, T, T_0 and $\dot{Q}$ bear their previous definitions, n is the normal vector of the surface, h is the heat convection coefficient, ε is the emissivity, σ is the Stefan-Boltzman constant which is $5.6704 \times 10^{-8} W/m^2K^4$, Γ represents the surfaces of the work piece and Λ represents the surface area irradiated by the laser beam.

2.1.3. Assumptions in the Finite Element Modeling. In order to simulate the thermal history during the laser metal deposition more efficiently and reduce the computational cost, some assumptions were taken into account. In the experiment, a Gaussian distributed laser beam was utilized to melt the substrate vertically with a non-uniform power

density. [14] Thus, the transverse intensity variation is described as (4):

$$I(r, y) = \alpha \frac{P}{\pi w(y)^2} exp\left(-2\frac{r^2}{w(y)^2}\right) \tag{4}$$

where α is the laser absorption coefficient, P is the power of the continuous laser, $w(y)$ and is the distance from the beam axis where the optical intensity drops to $1/e^2(\approx 13.5\%)$ of the value on the beam axis. α was set as 0.4 based on numerical experiments in the LAMP lab, and $w(y)$ is 1 mm in this simulation. The motion of laser beam was simulated by adjusting the position of beam center R with programming a user subroutine "DFLUX" in ABAQUS. The formula of R is as follows:

$$R = \left[\left(x - \int_{t_0}^{t} u \cdot dt\right) + \left(y - \int_{t_0}^{t} v \cdot dt\right) + \left(z - \int_{t_0}^{t} w \cdot dt\right)\right]^{1/2} \tag{5}$$

where x, y, and z are the spatial coordinates of the Gaussian laser beam center, and u, v, and w are the laser moving velocities.

The Marangoni effect caused by the thermocapillary phenomena can directly influence the temperature field in the whole domain, so it is taken into account to obtain more accurate thermal history during LMD. [2] The artificial thermal conductivity was put forward to addressing the Marangoni effect in the finite element method [15]

$$k_m(T) = \begin{cases} k(T), T \leq T_{liq} \\ 2.5k(T), T > T_{liq} \end{cases} \tag{6}$$

where k_m is the modified thermal conductivity, and T_{liq} is the liquidus temperature.

In the FEA model, the powder addition was simulated by activating elements in many steps.[16] The width of the deposit area is assumed to be the same as the Gaussian beam. The thickness of each layer is calculated by transverse speed, powder feed rate and absorption efficiency. The deposit geometry, boundary condition and heat flux was updated.

2.2. MICROSCOPIC CA MODEL

Heterogeneous nucleation occurs nearly instantaneously at a characteristic undercooling. The locations and crystallographic orientation of the new nuclei are randomly chosen at the surface or in the liquid. As explained by Oldfield [17], the continuous nucleation distribution, $dn/d\Delta T$',which characterizes the relationship between undercooling and the grain density, is described by a Gaussian distribution both at the mould wall and in the bulk liquid (7). The parameters of these two distributions, including maximum nucleation density , the mean undercooling , and the standard deviation of the grain density distribution , can be obtained from experiments and grain size measurements. The grain density, , is given by (7):

$$n\left(\Delta T\right)=\int_{0}^{\Delta T}\frac{dn}{d\Delta T'}d\Delta T'=\int_{0}^{\Delta T}\frac{n_{max}}{\Delta T_{\sigma}\sqrt[2]{2\pi}}exp\left[-\frac{1}{2}\frac{\Delta T'-\Delta T_{N}}{\Delta T_{\sigma}}\right]d\Delta T' \tag{7}$$

where n_{max} is the maximum nucleation density of nucleation grains, which is obtained by the integral of the nucleation distribution (from zero undercooling to infinite undercooling). ΔT_N and ΔT_σ are the mean undercooling and standard deviation of the grain density distribution, respectively. Here, all temperatures are in Kelvin.

Undercooling is the most important factor in the columnar and dendrite growth rate and grain size. The total undercooling of the dendritic tip consists of three parts: solute undercooling, thermal undercooling, and curvature undercooling. For most metallic alloys, the kinetic undercooling for atom attachment is small, so it is neglected [18]. The total undercooling can be calculated as follows:

$$\Delta T=mC_{0}\left[1-A(P_{C})\right]+\theta_{t}I(P_{t})+\frac{2\Gamma}{R} \tag{8}$$

where m is the liquidus slope; Γ is the Gibbs-Thomson coefficient; C_0 is the solute concentration in the liquid far from the solid-liquid interface; P_t and P_c are the thermal and solutal P*é*clet numbers, respectively; k is the solute partition coefficient at the solid-liquid interface; $A(P_C)$ equals $[1-(1-k)I(P_c)]^{-1}$; θ_t is the unit thermal undercooling ($=\Delta h_f/c$); and R is the radius of the dendritic tip.

For the laser deposition process, the rapid solidification condition corresponds to a high P*é*clet number at which the dendritic tip radius is given by (9)

$$R = [\frac{\Gamma}{\sigma^*(mG_c^* - G^*)}]^{1/2} \tag{9}$$

where, σ^*, the marginal stability constant, approximately equals $1/4\pi^2$ [19], G^* and G_c^* are the effective temperature gradient and concentration gradient, respectively.

2.3. COUPLING MACROSCOPIC FE AND MICROSCOPIC CA MODELS

The temperature field result can be used to calculate enthalpy increment, which is necessary to calculate enthalpy at each time step. A linearized implicit FE enthalpy formulation of the heat flow equation can be given by equation (10) in [7]

$$\left[\frac{1}{\Delta t}\cdot[M] + [K]^t[\frac{\partial T}{\partial H}]^t\right]\cdot\{\delta H\} = -\{K\}^t\cdot\{T\}^t + \{b\}^t \tag{10}$$

where $\{M\}$ is the mass matrix; $\{K\}$ is the conductivity matrix; $\{b\}$ is the boundary condition vector; and $\{T\}$ and $\{H\}$ are the temperature and enthalpy vectors at each node of the FE mesh, respectively. The Newton Method and Euler implicit iteration are included in (10). This set of equations can be solved using the Gauss elimination method for $\{\delta H\}$.

$$\delta H = \rho\cdot c_p\cdot[T^{t+\delta t} - T^t] - \Delta H_f\cdot\delta f_s \tag{11}$$

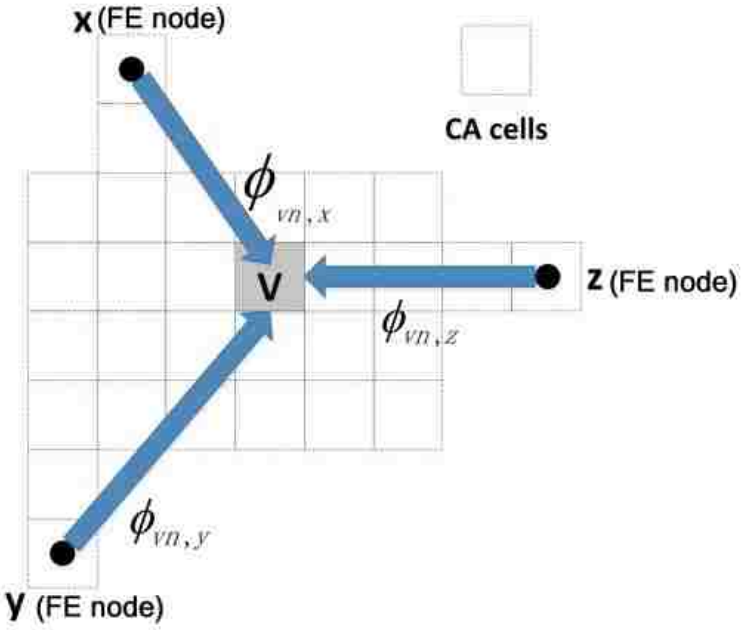

Figure 3. Interpolation schematic between FE and CA models

Thus, the next time-step enthalpy can be obtained by the relationship $H_i^{t+1} = H_i^t + \delta H$. The new temperature field can be obtained from the coupling model using (11). ΔH_f is the latent heat of fusion per unit volume. δf_s can be calculated as in [7].

In the FE macroscopic model, the temperature field was calculated on a relatively coarse mesh, but the solidification microstructure had to be developed on a finer regular CA mesh with a cell size of the order of the secondary dendrite arm spacing (SDAS). Figure 3 indicates the interpolate relationship between coarse FE nodes and fine CA cells. The known temperature T_n^t and the volumetric enthalpy variation δH_n were interpolated into the CA network by the linear interpolation in (12) and (13). ϕ_{vn} is the interpolation coefficient. Every CA cell temperature in the calculation domain can be obtained with this interpolation. In figure 3, x, y, and z represents the FE temperature nodes (coarse grids), and v represents the CA cells (fine grids). The three linear interpolation coefficients from FE nodes x, y, z

to CA cells v are $\phi_{vn,x}$, $\phi_{vn,y}$ and $\phi_{vn,z}$

$$T_v^t = \sum_n \phi_{vn} \cdot T_n^t \tag{12}$$

$$H_v^t = \sum_n \phi_{vn} \cdot H_n^t \tag{13}$$

The finer temperature, T_v^t, and enthalpy variations δH_v^t in regular CA cells were used in equation (13) to yield the temperature in the next micro time step. After a few micro time steps, the temperature field in the CA network could be substituted into the coarser nodes of the macroscopic model.

3. SIMULATION RESULTS

Figure 4 indicates the position of the deposition area on the substrate and the size of the substrate. The temperature-dependent thermal and mechanical properties of Ti-6Al-4V, including density, specific heat, thermal conductivity, and latent heat, are provided as input parameters for the FE model [13]. ABAQUS was used to simulate the temperature field of the substrate and deposited material, including the deposition materials added on the substrate when the laser moved forward and backward. The dimensions of the substrate are $2'' \times 0.5'' \times 0.25''$. A Fortran subroutine was written to simulate the Gaussian moving laser's heat source. The laser deposition of single layer Ti-6Al-4V was conducted with the power of 750 W, scanning speed of 600 mm/min and powder delivery of 12 g/min. The deposited material was added by activating elements in the deposition domain in a stepwise manner. All material properties were considered temperature-dependent shown in Table 1.

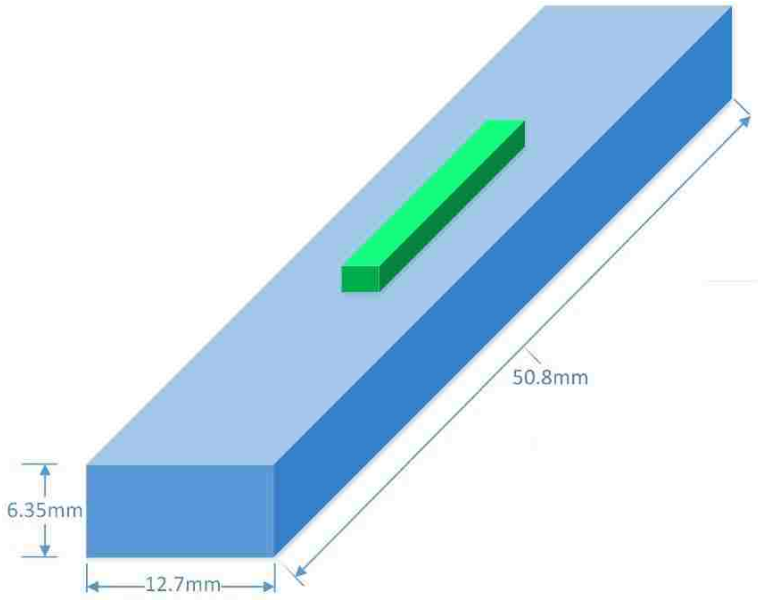

Figure 4. Ti-6Al-4V substrate dimension schematic

3.1. SOLIDIFICATION GRAIN MORPHOLOGY MODELING UNDER LASER DEPOSITION

The deposition temperature field and grain morphology were simulated first only in one layer. Figure 5 shows thermal history of the whole block during the LMD process. Figure 5(a) indicates the temperature field of the whole block when laser beam is passing along x direction at time = 1.0s. while Figure 5(b) shows the temperature field when substrate cools down with laser off at time = 29.0s. The total physical time of one-layer laser deposition is 2 s, while the cooling time is 28 s in the simulation. For each step, the step time is 0.1 s when the laser is shot on the surface of the deposited material. After 30 s cooling down, the temperature distribution is more uniform. Figure 6 indicates the thermal history of two nodes, which locate at the center point in the deposit and 1mm away from the deposit. The result shows that the highest temperature in the deposit is approximately 2884 K, which occurred at the center of the Gaussian beam. The center node at 1mm away from the deposit arrives at peak temperature of 1126K that cannot melt the Ti6Al4V

Table 1. Ti-6Al-4V temperature-dependent properties in the FE-CA simulation [13]

Temperature (K)	Thermal Conductivity ($W/(m \cdot K)$)	Density (kg/m^3)	Specific Heat ($J/(kg \cdot K)$)
300	5.9596	4419.7	547.54
500	9.1095	4388.9	590.54
700	12.2495	4358.1	633.54
900	15.3895	4327.3	676.54
1100	18.5295	4296.5	719.54
1300	20.0227	4265.7	646.83
1500	22.5627	4234.9	682.85
1700	25.1027	4204.1	718.87
1900	27.6427	4173.3	754.89
2100	37.648	3799.6	831
2300	42.448	3663.6	831
2500	47.248	3527.6	831
2700	52.048	3391.6	831
2900	56.848	3255.6	831

substrate. Based on every node's thermal history, the undercooling (discrepancy between liquidus temperature and current temperature) that is critical to resulting in grain nucleation and growth rate can be determined.

The thermal history during the whole deposition process can directly influence the grain structure and size distribution. The Figure 7 indicates that grain morphology simulation of single-layer deposition of Ti-6Al-4V. In the legend, 'CLASS' represents orientations of different grains. The four subfigures show 200ms solidification process. The domain size in the CA model was $2.0mm \times 0.4mm$, and the simulation time was 200 ms. The Y and Z axes are agreement with temperature field coordinates. The original temperature nodes obtained from ABAQUS were linearly interpolated because the element size in ABAQUS was $200\mu m$. The size of each cell was $10\mu m$ in the CA model. Different colors indicate individual grains. The grain nucleation sites and growth rate were controlled by the temperature history obtained from the FEA model. When it decreases to the liquidus temperature, nuclei appear at the random sites in the molten pool or at the interface between

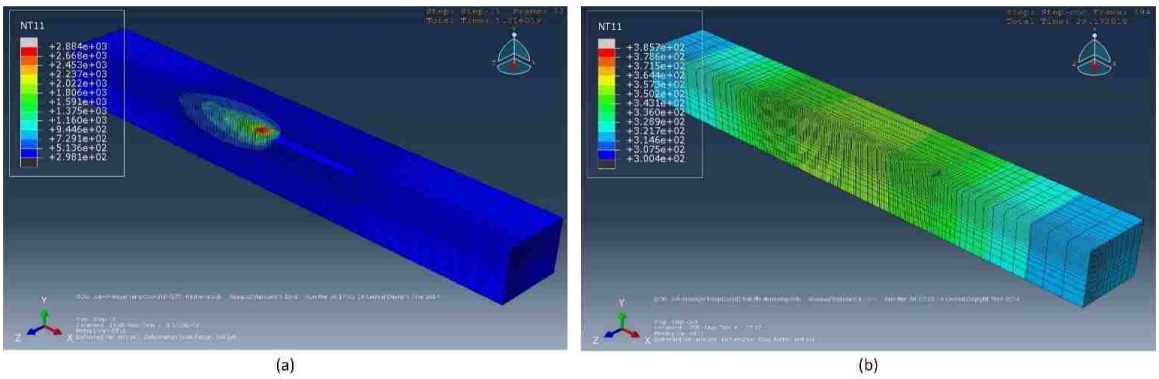

Figure 5. Cross sectional simulated temperature distribution during single-layer laser deposition process at (a) time = 1.0s (b) time = 29.0s

the solid and liquid. When the temperature continues to decrease, some nuclei grow along random orientation in a certain growth rate. Since the cooling rate is very high, a large amount of small grains form during the cooling process. For one-layer laser deposition microstructure simulation, the grains were almost equiaxed. The grain size varied from 30μm to 150μm. There are little columnar grains for one-layer laser deposition. Figure 8 depicts the temperature field of the substrate and deposited material, including the 25-layer deposition materials added on the substrate when the laser moved forward and backward. The laser deposition of multiple-layer Ti-6Al-4V was conducted with the power of 750 W, scanning speed of 200 mm/min, and powder delivery of 2 g/min. The elemental size is non-uniform along three directions since it is not necessary to apply fine elements to where the location is far from the molten pool. Figure 9 shows that the thermal history and peak temperature of different layers are not identical. The higher layer performs higher thermal history because the higher layer accumulates more heat than the lower one and it is closer to heat source. Figure 10 shows multiple layers of the Ti-6Al-4V grain morphology under the laser deposition process. In the legend, 'CLASS' represents orientations of different grains. Y and Z coordinates are in agreement with 25 layer thermal history result. Irregular grain shape and size can be obtained. When more layers were deposited, columnar grains began to dominate, while equiaxed grains began disappearing. As the solidification

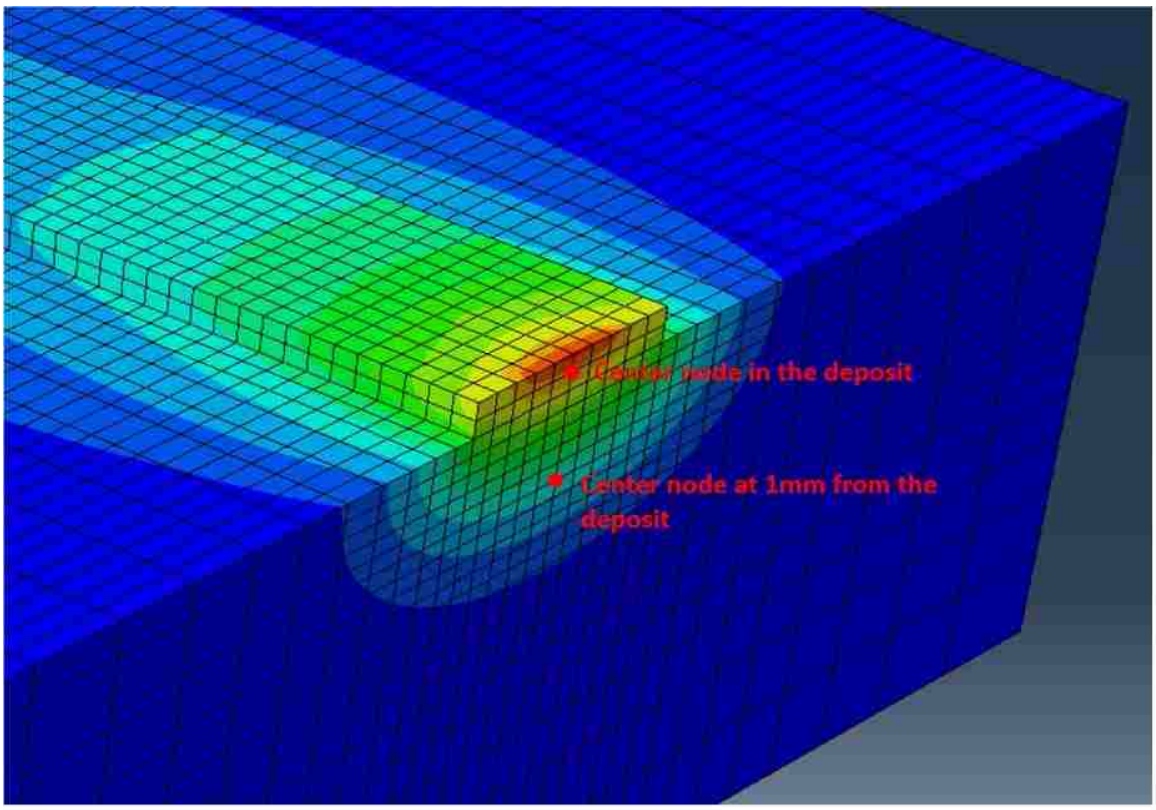

(a)

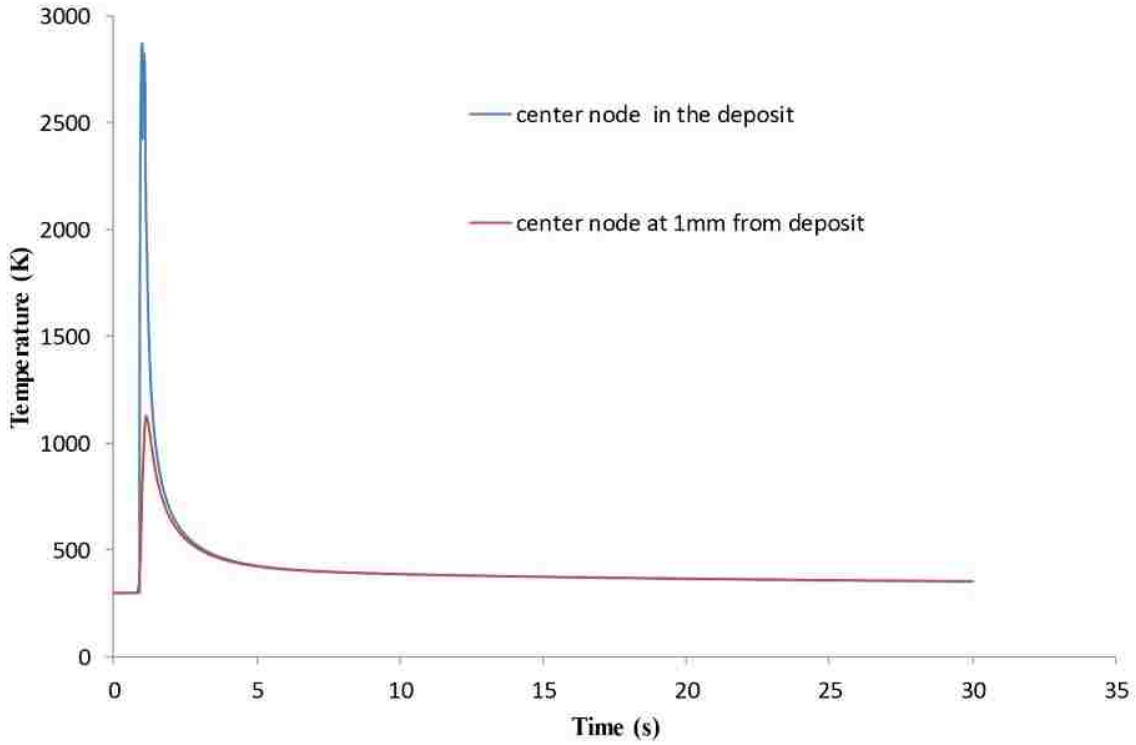

(b)

Figure 6. Temperature history at the center node in the deposit and substrate during deposition and cooling process

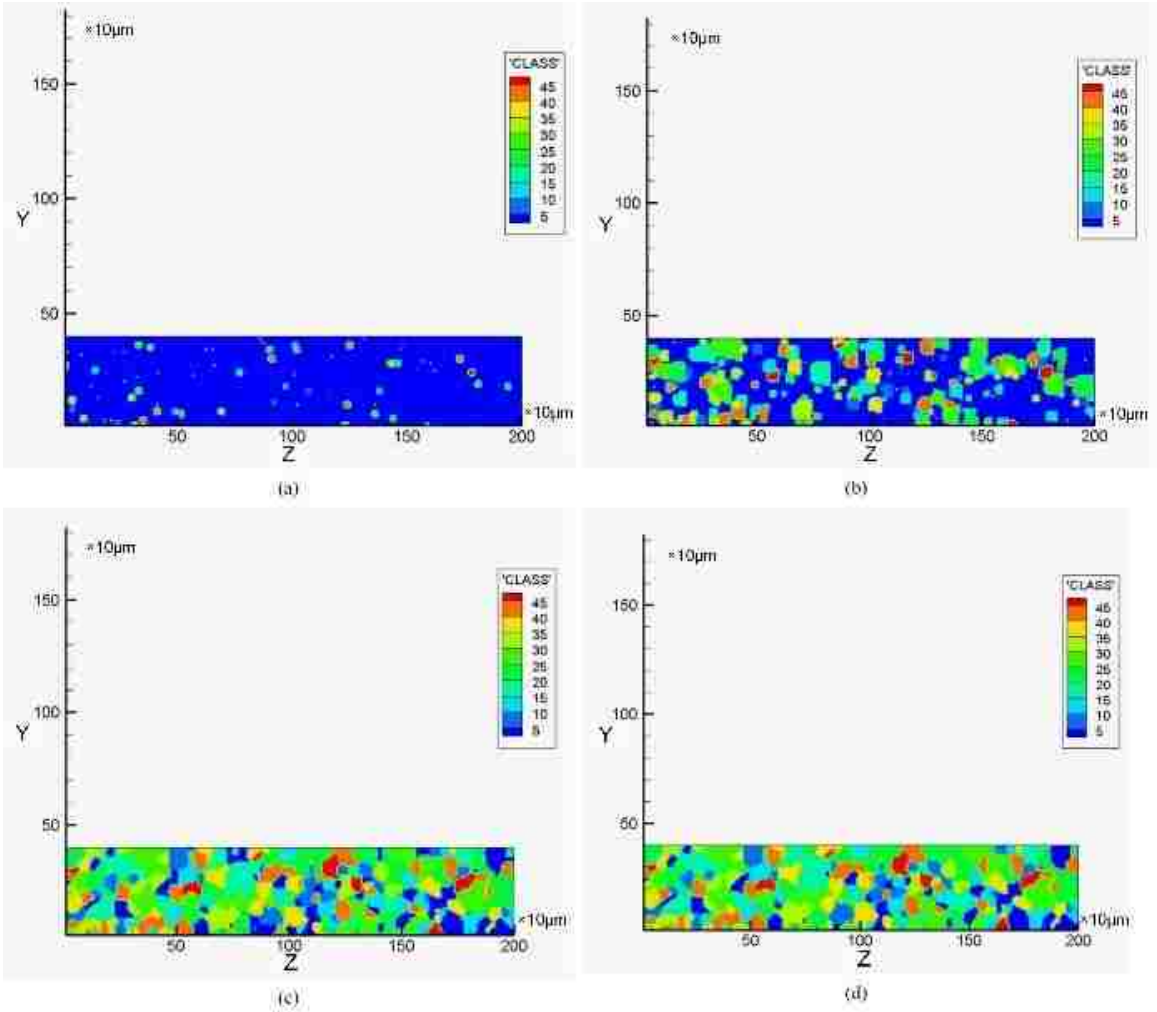

Figure 7. Grain morphology simulation of single-layer deposition of Ti-6Al-4V at (a) t=50ms, (b) t=100 ms, (c) t=150 ms, (d) t=200 ms

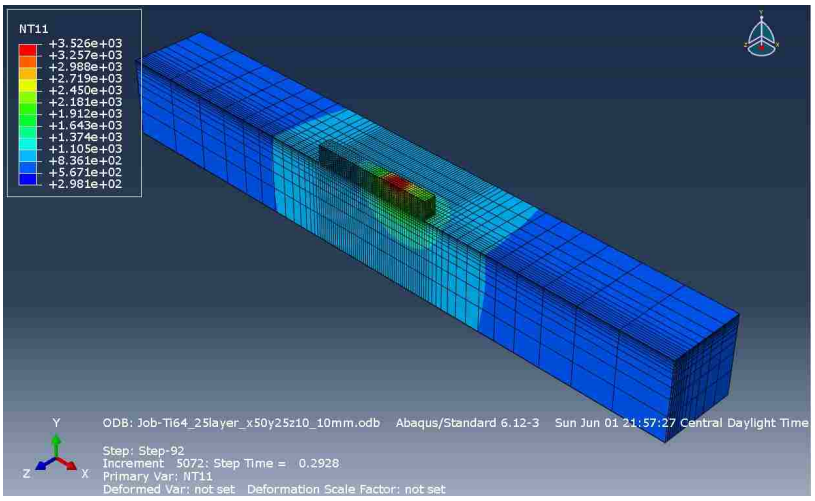

Figure 8. Thermal history for 25-layer Ti-6Al-4V laser deposition

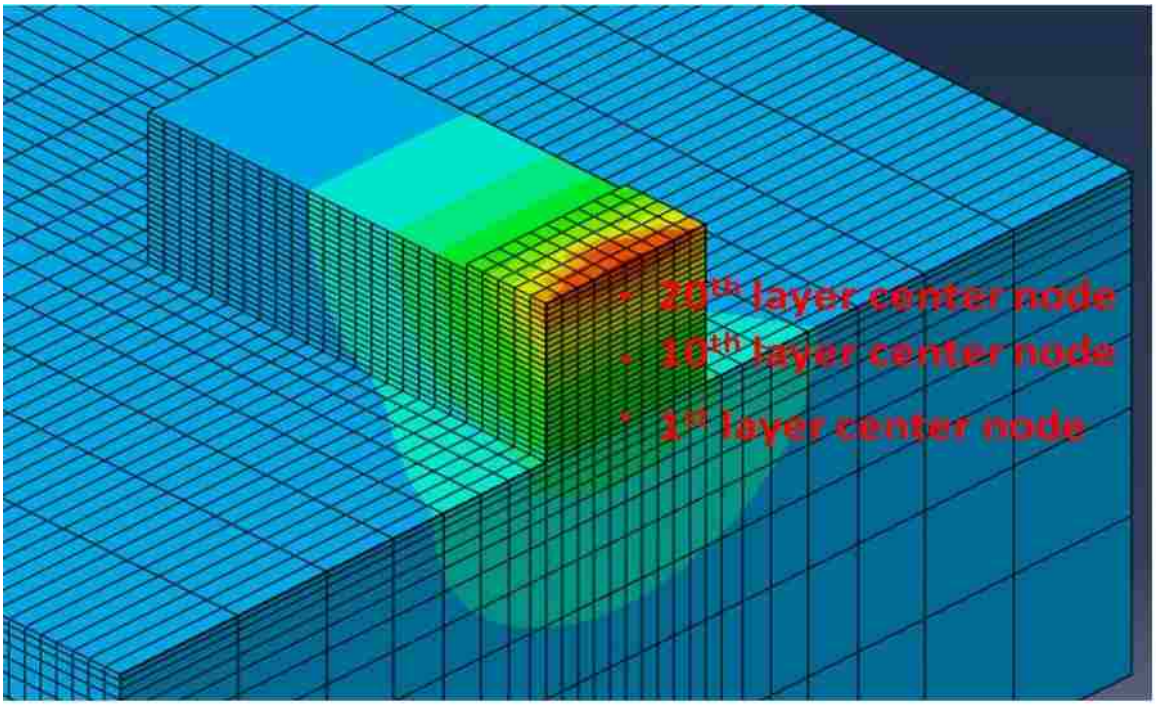

(a)

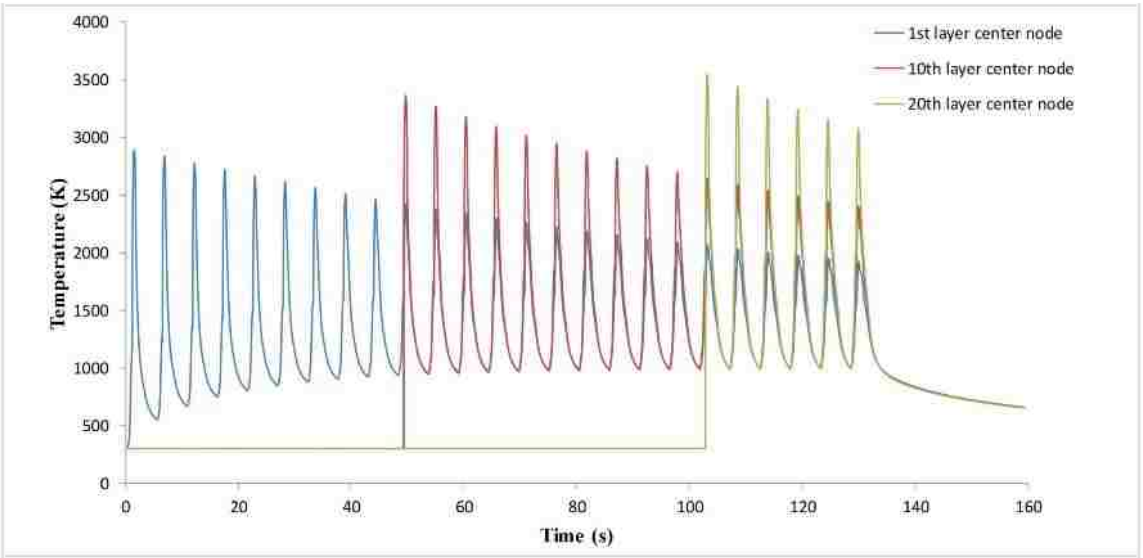

(b)

Figure 9. (a) Three nodes location cross-section schematic (b) Thermal history of the center node at 1st, 10th and 20th layer

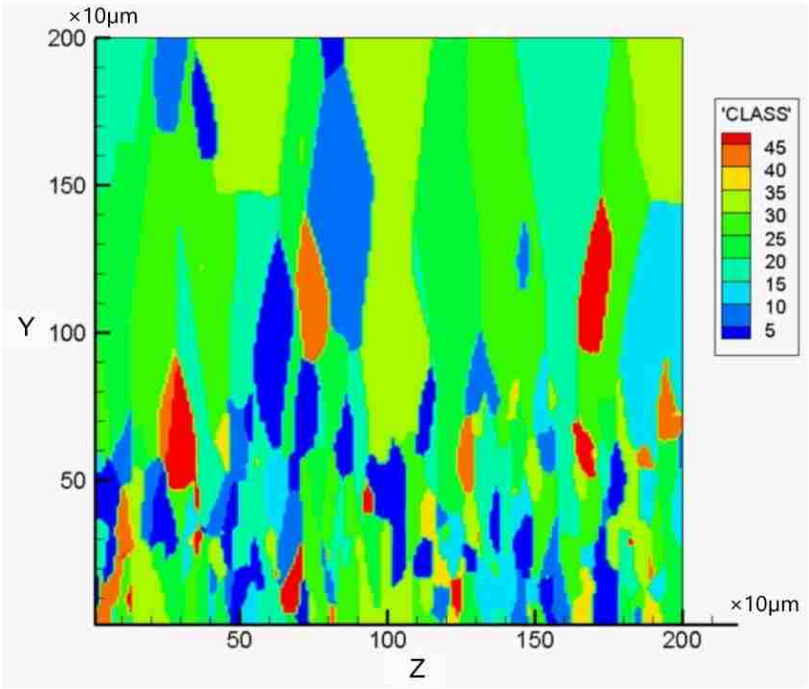

Figure 10. Grain morphology modeling of 25-layer Ti-6Al-4V laser deposition

process continues, competitive growth among different grains occurrs. Therefore, the size of columnar grain increases, and the number of grains goes down. The orientations of the columnar grains were almost perpendicular to the laser motion's direction because the grains grew along thermal gradient direction. The domain size in the CA model was $2mm \times 2mm$ Based on this cellular automaton simulation result, the width of the columnar grains varied from $100\mu m$ to $600\mu m$.

4. EXPERIMENTAL VALIDATION

4.1. MICROSTRUCTURE VALIDATION

A laser deposition experiment was conducted with the power of 750 W, scanning speed of 200 mm/min and 2g/min for 25 layer deposit. The powder absorption efficiency in the LAMP lab is about 0.3 âĂŞ 0.4 after the measurement. Figure 11 shows Ti-

6Al-4V deposition grain microstructure. The deposit region cross section dimension is $1.8mm \times 1.9mm$, which is close to $2mm \times 2mm$ assumption in the simulation. It can be observed that columnar grains dominate in the laser deposition area. Figure 12 (a) and (b) indicate the whole deposition region at different magnification and the locations of top and bottom region, while (c) and (d) shows the grain size and shape with higher magnification. In Figure 11, it can be observed that at the bottom deposition, crystallographic orientation is not only limited to the vertical direction. As deposit goes up, columnar grains along the steepest thermal gradient direction overgrow other grains, then dominate the microstructure. This phenomenon verifies the columnar grain orientation in the simulation result. Figure 12 shows the grain size measurement result at bottom and top region. The columnar grain size increases as the deposition goes up. After measurement, the grain size ranges from $75\mu m$ to $290\mu m$ and $420\mu m$ to $700\mu m$ at the bottom and top deposition, respectively. In the model, the columnar grain width varied from $60\mu m$ to $600\mu m$ within a $2mm \times 2mm$ domain. The current grain morphology modeling result is in the same order of magnitude as optical morphologies.

5. CONCLUSION

The transient temperature field of one-layer and multiple-layer deposition of Ti-6Al-4V was simulated with finite element method. The FE model provides the temperature at a relatively coarse scale and interpolation algorithm was used to scale the temperature field to match that of the CA model. The FE-CA model predicts grain morphology evolution as the deposition cools down. Hence, the instantaneous nucleation law, dendritic grain growth, and crystallographic orientation were modeled in this study. It has been found that the equiaxed grains dominated for one-layer deposition, while columnar grains dominated in the 25-layer deposition in the simulation. The grain size becomes larger when the position

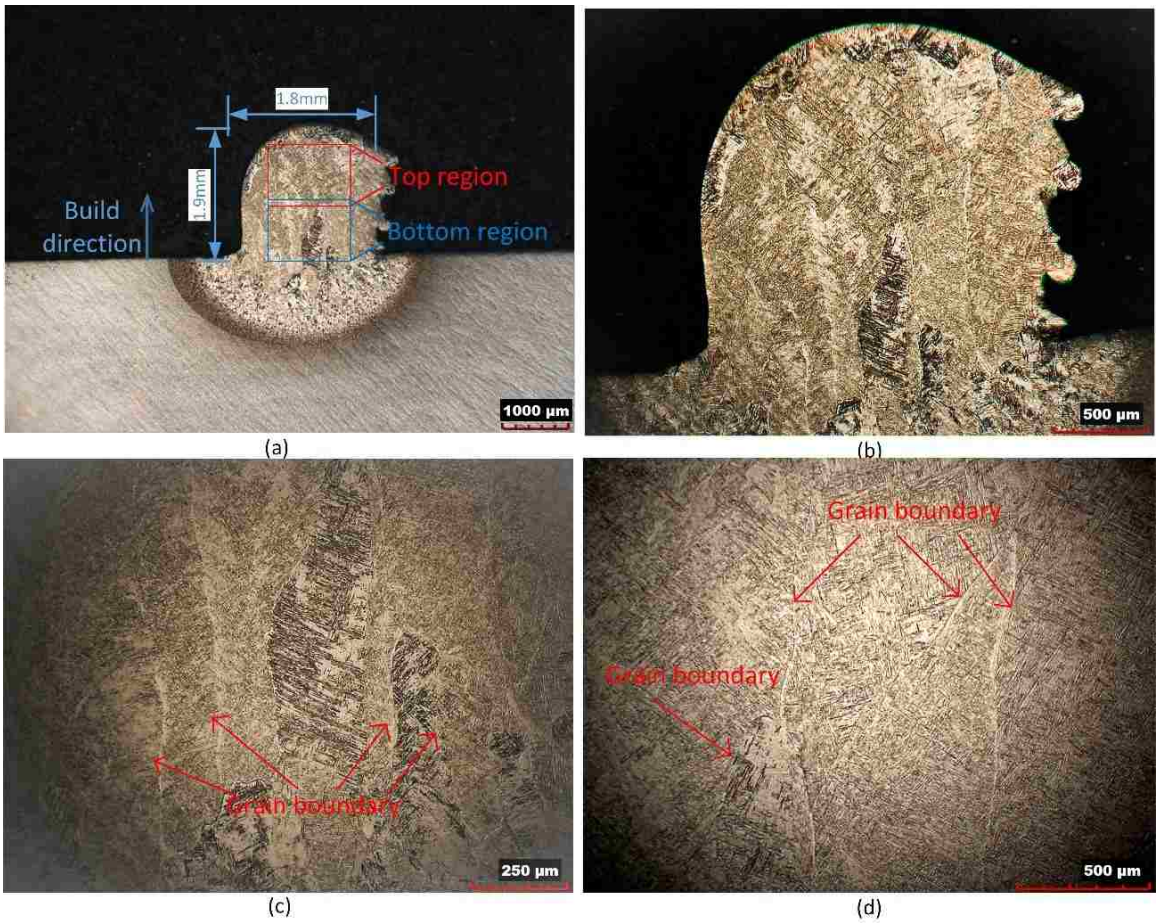

Figure 11. Ti-6Al-4V deposition grain morphologies at (a)(b) the whole deposition (c) the bottom region deposition (d) the top region deposition

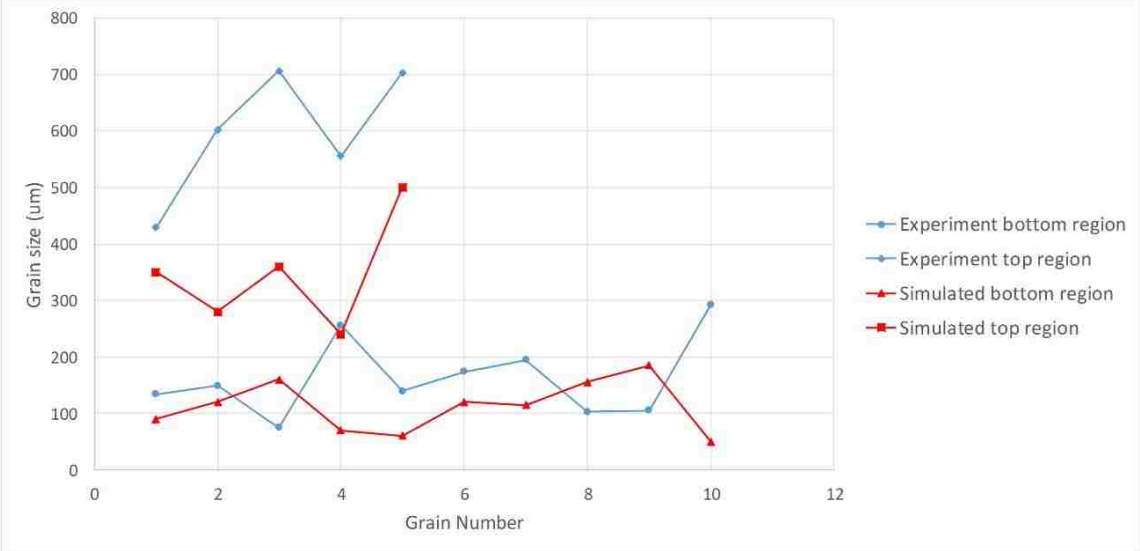

Figure 12. Simulated and experimental grain size measurement at bottom and top region

is closer to the top area of the deposition, which matches well with the microscopic result. It demonstrates that this FE-CA simulation can reasonably predict thermal history and grain morphology during this case of laser metal deposition.

REFERENCES

[1] Toyserkani, E., Khajepour, A., and Corbin, S., 2004, "3-D finite element modeling of laser cladding by powder injection: effects of laser pulse shaping on the process," Opt. Lasers Eng., 41(6), pp. 849-867.

[2] Alimardani, M., Toyserkani, E., and Huissoon, J. P., 2007, "A 3D dynamic numerical approach for temperature and thermal stress distributions in multilayer laser solid freeform fabrication process," Opt. Lasers Eng., 45(12), pp. 1115-1130.

[3] Anderson, M. P., Srolovitz, D. J., Grest, G. S., and Sahni, P. S., 1984, "Computer simulation of grain growth-I. Kinetics," Acta Metall., 32(5), pp. 783-791.

[4] Choudhury, A., Reuther, K., Wesner, E., August, A., Nestler, B., and Rettenmayr, M., 2012, "Comparison of phase-field and cellular automaton models for dendritic solidification in Al-Cu alloy," Comput. Mater. Sci., 55, pp. 263-268.

[5] Rappaz, M., and Gandin, C.-A., 1993, "Probabilistic modelling of microstructure formation in solidification processes," Acta Metall. Mater., 41(2), pp. 345-360.

[6] Raabe, D., 2002, "Cellular automata in materials science with particular reference to recrystallization simulation," Annu. Rev. Mater. Res., 32(1), pp. 53-6.

[7] Gandin, C.-A., and Rappaz, M., 1994, "A coupled finite element-cellular automaton model for the prediction of dendritic grain structures in solidification processes," Acta Metall. Mater., 42(7), pp. 2233-2246.

[8] Gandin, C.-A., Desbiolles, J.-L., Rappaz, M., and Thevoz, P., 1999, "A three-dimensional cellular automation-finite element model for the prediction of solidification grain structures," Metall. Mater. Trans. A, 30(12), pp. 3153-3165.

[9] Guillemot, G., Gandin, C.-A., and Combeau, H., 2006, "Modeling of Macrosegregation and Solidification Grain Structures with a Coupled Cellular Automaton-Finite Element Model," ISIJ Int., 46(6), pp. 880-895.

[10] Zhijian Wang, Shuai Luo, Hongwu Song, Weidong Deng, and Wenyi Li, 2014, "Simulation of Microstructure during Laser Rapid Forming Solidification Based on Cellular Automaton," Math. Probl. Eng., p. 9.

[11] L*ü*tjering, G., 1998, "Influence of processing on microstructure and mechanical properties of $\alpha + \beta$ titanium alloys," Mater. Sci. Eng. A, 243(1-2), pp. 32-45.

[12] Reddy, J. N., and Gartling, D. K., 2010, The finite element method in heat transfer and fluid dynamics, CRC PressI Llc.

[13] Kenneth C Mills, Recommended values of thermophysical properties for selected commercial alloys.

[14] Phillips, L. C. A. R. L., 2005, Laser Beam Propagation through Random Media, SPIE Publications.

[15] Lampa, C., Kaplan, A. F. H., Powell, J., and Magnusson, C., 1997, "An analytical thermodynamic model of laser welding," J. Phys. D. Appl. Phys., 30(9), p. 1293.

[16] Liu, H., and Sparks, T., 2012, "Modeling and verification of temperature distribution and residual stress in laser aided metal deposition process," (1), pp. 1-7.

[17] Oldfield, W., 1966, "A quantitative approach to casting solidification: Freezing of cast iron," Trans. Am. Soc. Met., 59, p. 945.

[18] D.J.FISHER, W. K. and, 1992, “Appendix 7 and 8,” Fundamentals of Solidification, TRANS TECH PUBLICATION, pp. 226-246.

[19] D.J.FISHER, W. K. and, 1992, “Appendix 9,” Fundamentals of Solidification, TRANS TECH PUBLICATION, pp. 247-260.

II. A TWO-DIMENSIONAL SIMULATION OF GRAIN STRUCTURE GROWTH WITHIN SUBSTRATE AND FUSION ZONE DURING DIRECT METAL DEPOSITION

Jingwei Zhang[a], Frank Liou[a], William Seufzer[a], Karen Taminger[a]

[a]Department of Mechanical & Aerospace Engineering

Missouri University of Science and Technology

Rolla, Missouri 65409–0050

ABSTRACT

In this paper, a predictive multi-scale model based on a cellular automaton (CA)-finite element (FE) method has been developed to simulate thermal history and microstructure evolution during metal solidification for Direct Metal Deposition (DMD) process. The macroscopic FE calculation that is validated by thermocouple experiment is developed to simulate the transient temperature field and cooling rate of single layer and multiple layers. In order to integrate the different scales, a CA-FE coupled model is developed to combine with thermal history and simulate grain growth. In the mesoscopic CA model, heterogeneous nucleation sites, grain growth orientation and rate, epitaxial growth, re-melting of pre-existing grains, metal addition, grain competitive growth, and columnar to equiaxed phenomena are simulated. The CA model is able to show the entrapment of neighboring cells and the relationship between undercooling and the grain growth rate. The model predicts the grain size, and morphological evolution during the solidification phase of the deposition process. The developed "decentered polygon" growth algorithm is appropriate for the non-uniform temperature field. Finally, the single and multiple-layer DMD experiment is conducted to validate the characteristics of grain features in the simulation.

Keywords: finite element, cellular automata, grain morphology, direct metal deposition, decentered polygon algorithm

1. INTRODUCTION

Compared with the conventional subtractive manufacturing technologies, additive manufacturing (AM) has unique advantages including low heat input, small heat-affected zone, solid-free-form fabrication, near-net-shape, and so on. Direct Metal Deposition (DMD), a rapid developing AM technique, is able to manufacture a fully dense metal part without intermediate steps, which is especially appropriate for the heterogeneous components manufacturing. During the deposition process, solidification thermodynamics determined by a series of process parameters affect microstructure evolution, which directly affects materials mechanical properties. The temperature field history and the cooling rate is the key factor to controlling the solidification microstructure after DMD process [1]. Several approaches, including stochastic and deterministic, have been taken to model solidification microstructure evolution. Anderson et al. [2, 3] developed a Monte Carlo (MC) stochastic method to simulate the grain growth, topology, grain size distribution, curvature and grain velocities, as well as their interrelationships. Saito and Enomoto [4] incorporated the anisotropy of the grain boundary energy, the pinning effect of precipitates on growth kinetics into the MC simulation. Another idea of modeling is the deterministic approach. Chen [5] investigated a phase field (PF) method to model and predict mesoscale morphological and microstructure evolution in materials. Krill et al. [6–8] developed PF to simulate 2D grain growth, 3D gain growth, equiaxed solidification. However, a phase field model usually carries a very high computational cost because of a requirement for a particularly fine computational grid.

In order to reduce the computational cost, RAPPAZ and GANDIN [9] put forward a two dimensional cellular automaton approach to model the grain structure formation in the solidification process. The model includes the mechanisms of heterogeneous nucleation

and of grain growth. Nucleation occurring at the interface as well as in the liquid metal is treated by using two distributions of nucleation sites. The location and the crystallographic orientation of the grains are chosen randomly among a large number of cells and a certain number of orientation classes, respectively. However, the model was then applied to small Al–7wt%Si specimens of uniform temperature. In order to develop the non-uniform temperature prediction, GANDIN et al [10] proposed a 2-dimensional Cellular Automaton (CA) technique for the simulation of dendritic grain formation during solidification. The non-uniform temperature situation was fully coupled to an enthalpy- based Finite Element (FE) heat flow calculation. This progress made it possible to combine the temperature field history with the microstructure evolution. The coupled CA-FE model is applied to A1-7wt% Si alloy. A three dimensional CA-FE model was analyzed of prediction of dendritic grain structures formed during solidification [11]. The potentiality of the CA-FE model is demonstrated through the predictions of typical grain structures formed during the investment casting and continuous casting processes. Based on the features of several developing approaches, Choudhury et al [12] compared a CA model with a PF model for simulations of dendritic solidification of an Al–4wt%Cu alloy, two- and three-dimensionally at different undercooling. In 2D, the PF model shows an excellent agreement of the simulated tip properties. At high undercooling, the CA model becomes advantageous, as its reproduction of the theoretical behavior improves. As the CA model is capable of simulating at coarse scales in a comparably short time, its output can be used as input for a PF simulation for resolving finer details of microstructure formation. This can be utilized to build a hybrid model to integrate CA high efficiency and PF accuracy. Dore [13] investigated quantitative prediction of micro-segregation during solidification of the ternary alloy system, which is applied to solidification of Al–Mg–Si. Jarvis et al [14] firstly compared 1D, 2D and 3D cellular automaton finite difference (CA-FD) simulations of non-

equilibrium solidification in Al–3.95Cu–0.8Mg ternary alloy. It has been demonstrated that there is good agreement between all CA-FD models in terms of primary α–Al phase. However, final dendrite arm spacings of 2D and 3D are slightly overestimated.

High cooling rate and non-equilibrium is a typical characteristic of DMD technique comparing conventional casting process and simulation. Grujicic et al. [15] proposed a modified CA-based method to investigate the evolution of solidification grain microstructure during LENS rapid fabrication process. This research established the relationship between process parameters (e.g. laser power, laser velocity) and solidification microstructure in binary metallic alloy. The finite difference analysis was also coupled with the modified CA to calculate the temperature field as the input of microstructure prediction. Kelly et al. [16, 17] developed the thermal history in DMD of Ti6Al4V and microstructural characterization. However, there is few investigation on microstructure evolution prediction based on whole deposit part during DMD process. This part-level simulation on microstructure is critical because it provides the foundation for mechanical properties prediction and control.

In this study, a predictive multi-scale model based on a Cellular Automaton (CA)-Finite Element (FE) method has been developed to simulate thermal history and microstructure evolution during metal solidification for a laser-based additive manufacturing process. ABAQUS was used to calculate the temperature field of the whole part, which offers the macroscopic FE nodes' temperature. In order to integrate the different scales, a coupled model is developed to combine with thermal history and simulate nucleation site, grain growth orientation and rate, epitaxial growth of new grains, remelting of preexisting grains, metal addition, and grain competitive growth. Interpolation was utilized to obtain the finer nodes' temperature based on the FE nodes result. The temperature field was validated by the type K thermocouples. The CA model, which was able to show the entrapment of neighboring cells and the relationship between undercooling and the grain growth rate, was built to simulate the microstructure information, such as the grain size and columnar grain orientation. The developed "decentered polygon" algorithm is more appropriate for

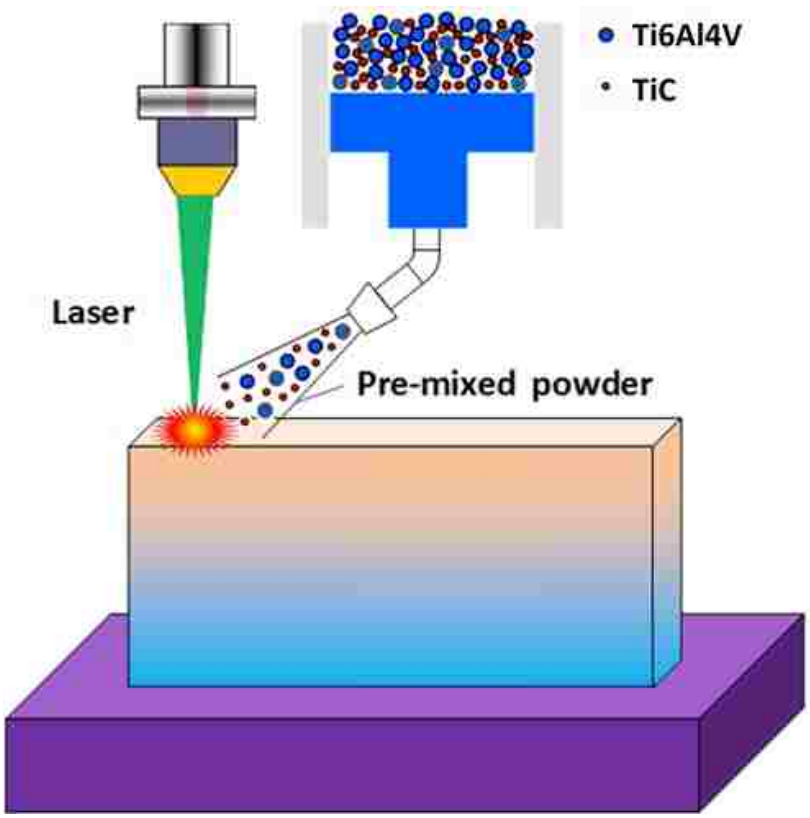

Figure 1. Laser powder deposition schematic

grain structure development in the highly non-uniform temperature field. This simulation will lead to new knowledge that simulates the grain structure development of single-layer and multiple-layer deposition during DMD process. The microstructure simulation results were validated by the experiment. The model parameters for the simulations were based on Ti-6Al-4V material.

2. MATHEMATICAL MODEL

2.1. TI6AL4V TRANSIENT TEMPERATURE FIELD DURING THE DEPOSITION PROCESS

In the Direct Metal Deposition (DMD) process, the temperature history of the whole domain directly influences the deposition microstructure, which is critical to mechanical properties [18]. In order to obtain the microstructure information during the solidification process, the temperature field must be known at each time step. The transient temperature field throughout the domain was obtained by solving the 3D heat conduction Eq (1), in the substrate, along with the appropriate initial and boundary conditions [19].

$$\rho(T) \cdot c_p(T) \cdot \frac{\partial T}{\partial t} = \frac{\partial}{\partial x}\left(k(T)\frac{\partial T}{\partial x}\right) + \frac{\partial}{\partial y}\left(k(T)\frac{\partial T}{\partial y}\right) + \frac{\partial}{\partial z}\left(k(T)\frac{\partial T}{\partial z}\right) + \dot{Q} \tag{1}$$

where T is the temperature, $\rho(T)$ is the density, $c_p(T)$ is the specific heat, $k(T)$ is the heat conductivity, and $\dot{Q}$ is the internal heat generation following certain energy distribution per unit volume.

The initial conditions applied to solve Eq (1) were:

$$T\,(x, y, z, 0) = T_0 \tag{2a}$$

$$T\,(x, y, z, \infty) = T_0 \tag{2b}$$

where T_0 is the ambient temperature. In this study, T_0 was set as room temperature, 298 K. The boundary conditions, including thermal convection and radiation, are described by Newton's law of cooling and the Stefan-Boltzmann law, respectively. The laser heating source term $\dot{Q}$, in (1), also was considered in the boundary conditions as a surface heat source. The boundary conditions then could be expressed as (3a)

$$K\,(\Delta T \cdot n)\,|_\Gamma = \left[-h\,(T - T_0) - \varepsilon\,(T)\,\sigma\left(T_0^4 - T_0\right)\right]\,|_\Gamma, \Gamma \notin \Lambda \tag{3a}$$

$$K\left(\Delta T \cdot n\right)|_{\Gamma} = \left[Q - h\left(T - T_0\right) - \varepsilon\left(T\right)\sigma\left(T_0^4 - T_0\right)\right]|_{\Gamma}, \Gamma \in \Lambda \tag{3b}$$

where k, T, T_0 and $\dot{Q}$ bear their previous definitions, n is the normal vector of the surface, h is the heat convection coefficient, ε is the emissivity, σ is the Stefan-Boltzman constant which is $5.6704 \times 10^{-8} W/m^2K^4$, Γ represents the surfaces of the work piece and Λ represents the surface area irradiated by the laser beam.

In order to simulate the thermal history during the laser metal deposition more efficiently and reduce the computational cost, some assumptions were taken into account. In the experiment, a Gaussian distributed laser beam was utilized to melt the substrate vertically with a non-uniform power density. [20] Thus, the transverse intensity variation is described as Eq (4)

$$I(r, y) = \alpha \frac{P}{\pi w(y)^2} exp\left(-2\frac{r^2}{w(y)^2}\right) \tag{4}$$

where α is the laser absorption coefficient, P is the power of the continuous laser, $w(y)$ and is the distance from the beam axis where the optical intensity drops to $1/e^2 (\approx 13.5\%)$ of the value on the beam axis. α was set as 0.4 based on numerical experiments in the LAMP lab, and $w(y)$ is 1 mm in this simulation. The motion of laser beam was simulated by adjusting the position of beam center R with programming a user subroutine "DFLUX" in ABAQUS. The formula of R is as follows:

$$R = \left[\left(x - \int_{t_0}^{t} u \cdot dt\right) + \left(y - \int_{t_0}^{t} v \cdot dt\right) + \left(z - \int_{t_0}^{t} w \cdot dt\right)\right]^{1/2} \tag{5}$$

where x, y, and z are the spatial coordinates of the Gaussian laser beam center, and u, v, and w are the laser moving velocities.

The Marangoni effect caused by the thermocapillary phenomena can directly influence the temperature field in the whole domain, so it is taken into account to obtain more accurate thermal history during DMD. [21] The artificial thermal conductivity was

put forward to addressing the Marangoni effect in the finite element method [22]

$$k_m(T) = \begin{cases} k(T), T \leq T_{liq} \\ 2.5k(T), T > T_{liq} \end{cases} \tag{6}$$

where k_m is the modified thermal conductivity, and T_{liq} is the liquidus temperature.

In the FEA model, the powder addition was simulated by activating elements in many small steps.[23] The width of the deposit area is assumed to be the same as the Gaussian laser beam. The thickness of each layer is calculated by transverse speed, powder feed rate and powder absorption efficiency. The deposit geometry, boundary condition and heat flux was updated after each step.

2.2. TI6AL4V MORPHOLOGY PREDICTION AFTER SOLIDIFICATION

Heterogeneous nucleation occurs nearly instantaneously at a characteristic undercooling. The locations and crystallographic orientation of the new nuclei are randomly chosen at the surface or in the liquid. As explained by Oldfield [24], the continuous nucleation distribution, $dn/d\Delta T$,which characterizes the relationship between undercooling and the grain density, is described by a Gaussian distribution both at the mould wall and in the bulk liquid. The parameters of these two distributions, including maximum nucleation density n_{max} , the mean undercooling ΔT_N, and the standard deviation of the grain density distribution ΔT_σ , can be obtained from experiments and grain size measurements. The grain density, $n(\Delta T)$, is given by Eq (7):

$$n(\Delta T) = \int_0^{\Delta T} \frac{dn}{d\Delta T'} d\Delta T' = \int_0^{\Delta T} \frac{n_{max}}{\Delta T_\sigma \sqrt[2]{2\pi}} exp\left[-\frac{1}{2}\frac{\Delta T' - \Delta T_N}{\Delta T_\sigma}\right] d\Delta T' \tag{7}$$

where n_{max} is the maximum nucleation density of nucleation grains, which is obtained by the integral of the nucleation distribution (from zero undercooling to infinite undercooling). ΔT_N and ΔT_σ are the mean undercooling and standard deviation of the grain density distribution, respectively. Here, all temperatures are in Kelvin.

Undercooling is the most important factor in the columnar and dendrite growth rate and grain size. The total undercooling of the dendritic tip consists of three parts: solute undercooling, thermal undercooling, and curvature undercooling. For most metallic alloys, the kinetic undercooling for atom attachment is small, so it is neglected [25]. The total undercooling can be calculated as follows:

$$\Delta T = mC_0\,[1 - A(P_C)] + \theta_t I(P_t) + \frac{2\Gamma}{R} \tag{8}$$

where m is the liquidus slope; Γ is the Gibbs-Thomson coefficient; C_0 is the solute concentration in the liquid far from the solid-liquid interface; P_t and P_c are the thermal and solutal P*é*clet numbers, respectively; k is the solute partition coefficient at the solid-liquid interface; $A(P_C)$ equals $[1 - (1 - k)I(P_c)]^{-1}$; θ_t is the unit thermal undercooling ($= \Delta h_f/c$); and R is the radius of the dendritic tip.

For the laser deposition process, the rapid solidification condition corresponds to a high P*é*clet number at which the dendritic tip radius is given by (9)

$$R = [\frac{\Gamma}{\sigma^*(mG_c^* - G^*)}]^{1/2} \tag{9}$$

where, σ^*, the marginal stability constant, approximately equals $1/4\pi^2$ [26], G^* and G_c^* are the effective temperature gradient and concentration gradient, respectively.

2.3. COUPLING MACROSCOPIC FE AND MESOSCOPIC CA MODELS

The temperature field result can be used to calculate enthalpy increment, which is necessary to calculate enthalpy at each time step. A linearized implicit FE enthalpy formulation of the heat flow equation can be given by equation (10) in Ref [10]

$$\left[\frac{1}{\Delta t}\cdot[M]+[K]^t[\frac{\partial T}{\partial H}]^t\right]\cdot\{\delta H\}=-\{K\}^t\cdot\{T\}^t+\{b\}^t \tag{10}$$

where $\{M\}$ is the mass matrix; $\{K\}$ is the conductivity matrix; $\{b\}$ is the boundary condition vector; and $\{T\}$ and $\{H\}$ are the temperature and enthalpy vectors at each node of the FE mesh, respectively. The Newton Method and Euler implicit iteration are included in (10). This set of equations can be solved using the Gauss elimination method for $\{\delta H\}$.

$$\delta H=\rho\cdot c_p\cdot[T^{t+\delta t}-T^t]-\Delta H_f\cdot\delta f_s \tag{11}$$

Thus, the next time-step enthalpy can be obtained by the relationship $H_i^{t+1}=H_i^t+\delta H$. The new temperature field can be obtained from the coupling model using (11). ΔH_f is the latent heat of fusion per unit volume. δf_s can be calculated as in [10].

In the FE macroscopic model, the temperature field was calculated on a relatively coarse mesh, but the solidification microstructure had to be developed on a finer regular CA mesh with a cell size of the order of the secondary dendrite arm spacing (SDAS). Figure 2 indicates the interpolate relationship between coarse FE nodes and fine CA cells. The known temperature T_n^t and the volumetric enthalpy variation δH_n were interpolated into the CA network by the linear interpolation in (12) and (13). ϕ_{vn} is the interpolation coefficient. x, y, and z represents the FE temperature nodes (coarse grids), and v represents the CA cells (fine grids). The three linear interpolation coefficients from FE nodes x, y, z to CA cells v are $\phi_{vn,x}$, $\phi_{vn,y}$ and $\phi_{vn,z}$. Every CA cell temperature in the calculation domain can

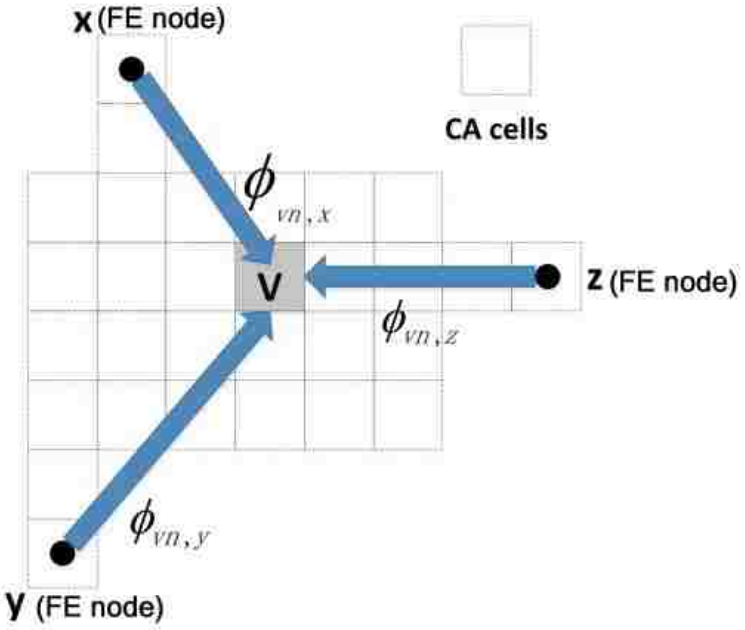

Figure 2. Interpolation schematic between FE and CA models

be obtained with this interpolation.

$$T_v^t = \sum_n \phi_{vn} \cdot T_n^t \tag{12}$$

$$H_v^t = \sum_n \phi_{vn} \cdot H_n^t \tag{13}$$

The finer temperature, T_v^t, and enthalpy variations δH_v^t in regular CA cells were used in Eq (13) to yield the temperature in the next micro time step. After a few micro time steps, the temperature field in the CA network could be substituted into the coarser nodes of the macroscopic model. The interpolated temperature field is employed as the model input. Heterogeneous nucleation, grain growth orientation, and grain growth are solved in the CA-FE model in terms of nucleation location distribution, random crystallographic orientation, and CA cells capture. Figure 3 indicates the flow chart of coupling FE-CA model. The details of CA growth algorithm are shown in Figure 4.

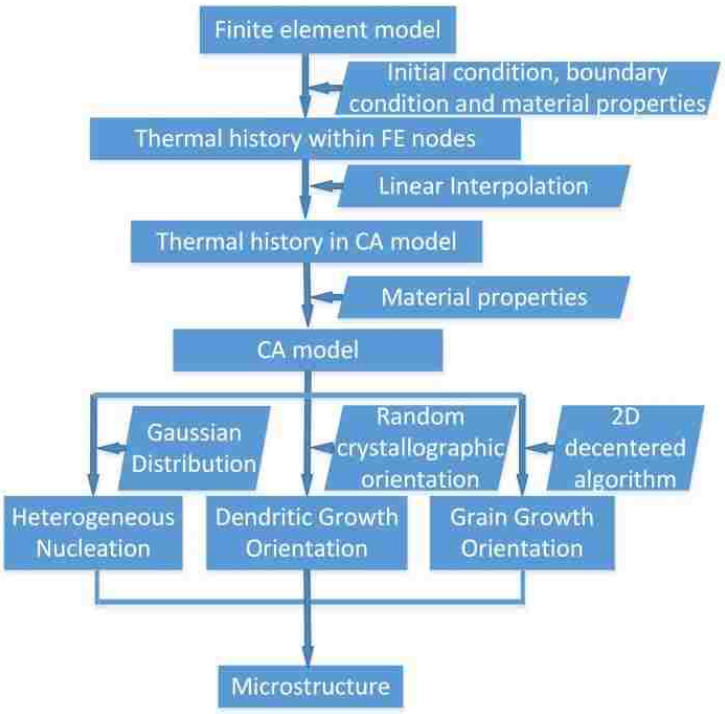

Figure 3. Flow chart of the coupling CA-FE model

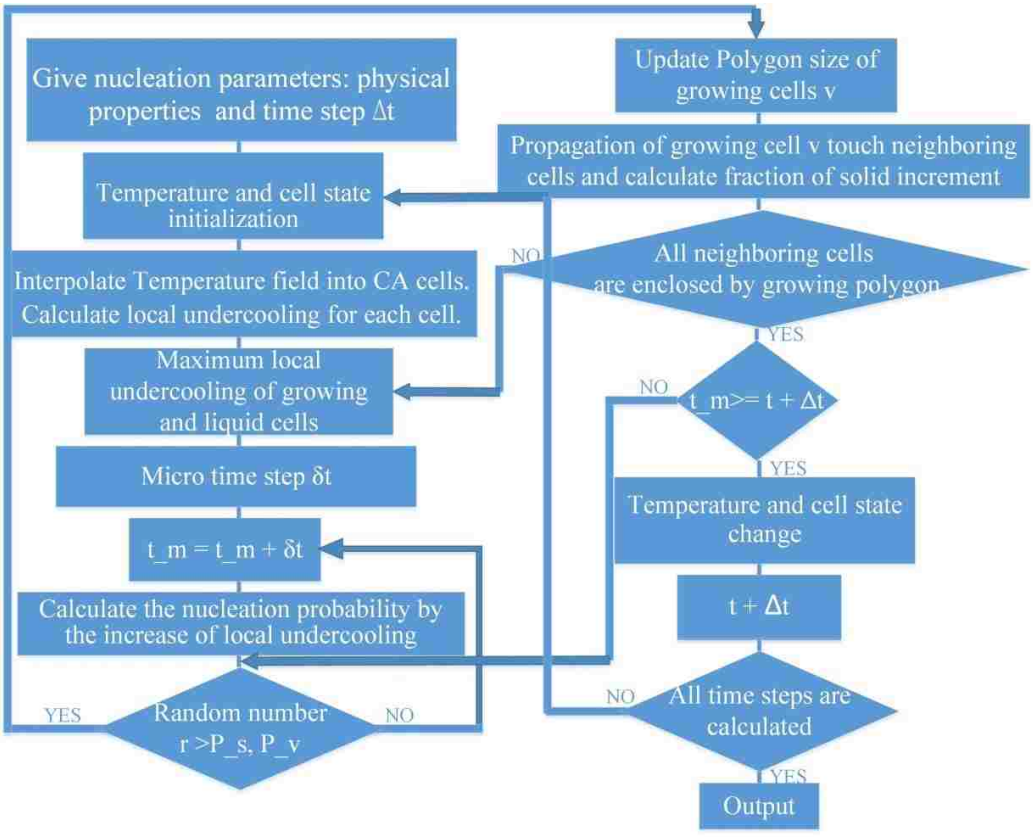

Figure 4. Flow chart of CA algorithm

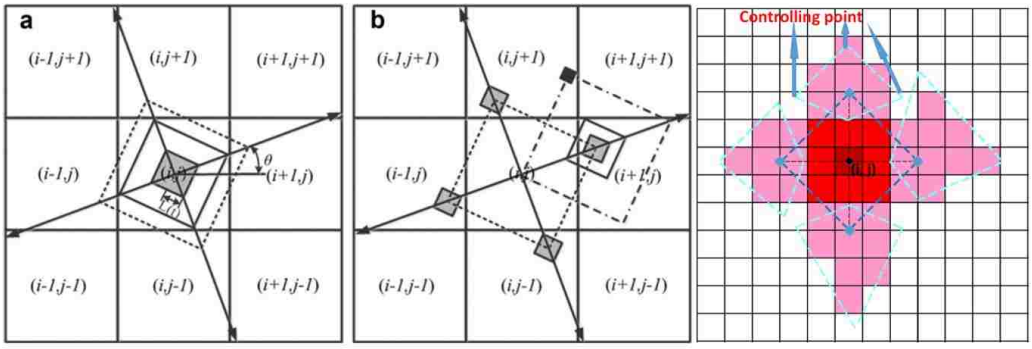

Figure 5. Illustration of the conventional and modified cell capture algorithm: (a) capturing rule of cell (i, j) within a decentered square, (b) capturing rule of 8 neighboring cells before (i, j) growth termination [27], (c) the modified cell capture and growth algorithm of "Decentred Polygon" with neighboring cells effect for cubic crystal alloys

Figure 5 illustrates the conventional and modified cell capture algorithm. For the conventional method, the vertices of the square envelope moves along the diagonal, and the growth of the square envelope is determined by the center cell temperature, not local temperature, at each time step, which results in the same growth rate for the four vertices. The grain orientation will be along with the axis of computational domain after a few time steps, thus losing its original orientation information. The modified "Decentered Polygon" algorithm is implemented to control the grain growth within melt pool and at the sold/liquid interface. Compared to the traditional "decentered square" algorithm of cell capturing, the modified "decentered polygon" algorithm does not need to create square for each cell when it begins to grow. Only the decentered polygon of a starting nucleated cell is tracked during the grain growth process, which reduces the computation cost. Besides, the modified algorithm can prevent grain orientations from realigning with x axis after a few growing steps because each cell will stop growing when Von Neumann and Moore neighbors are both solid. The controlling point growth rate is determined by the local cell temperature. Therefore, the region with higher thermal gradient will solidify faster along the steepest thermal gradient.

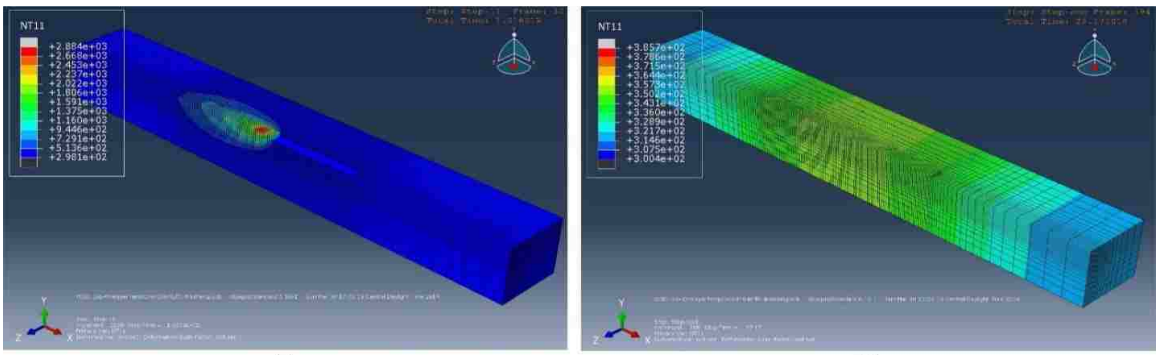

Figure 6. Cross sectional simulated temperature distribution during single-layer laser deposition process at (a) time = 1.0s (b) time = 29.0s

3. RESULTS AND DISCUSSION

3.1. SINGLE-LAYER TEMPERATURE AND GRAIN STRUCTURE

The deposition temperature field and grain morphology were simulated first only in one layer. Ti6Al4V properties are shown in Table 1. Figure 6 shows thermal history of the whole block during the DMD process. Figure 6(a) indicates the temperature field of the whole block when laser beam is passing along x direction at time = 1.0s. while Figure 6(b) shows the temperature field when substrate cools down with laser off at time = 29.0s. The total physical time of one-layer laser deposition is 2 s, while the cooling time is 28 s in the simulation. For each step, the step time is 0.1 s when the laser is shot on the surface of the deposited material. After 30 s cooling down, the temperature distribution is more uniform. Figure 7 indicates the thermal history of two nodes, which locate at the center point in the deposit and 1mm away from the deposit. The result shows that the highest temperature in the deposit is approximately 2884 K, which occurred at the center of the Gaussian beam. The center node at 1mm away from the deposit arrives at peak temperature of 1126K that cannot melt the Ti6Al4V substrate. Based on every node's thermal history, the undercooling (discrepancy between liquidus temperature and current temperature) that is critical to resulting in grain nucleation and growth rate can be determined.

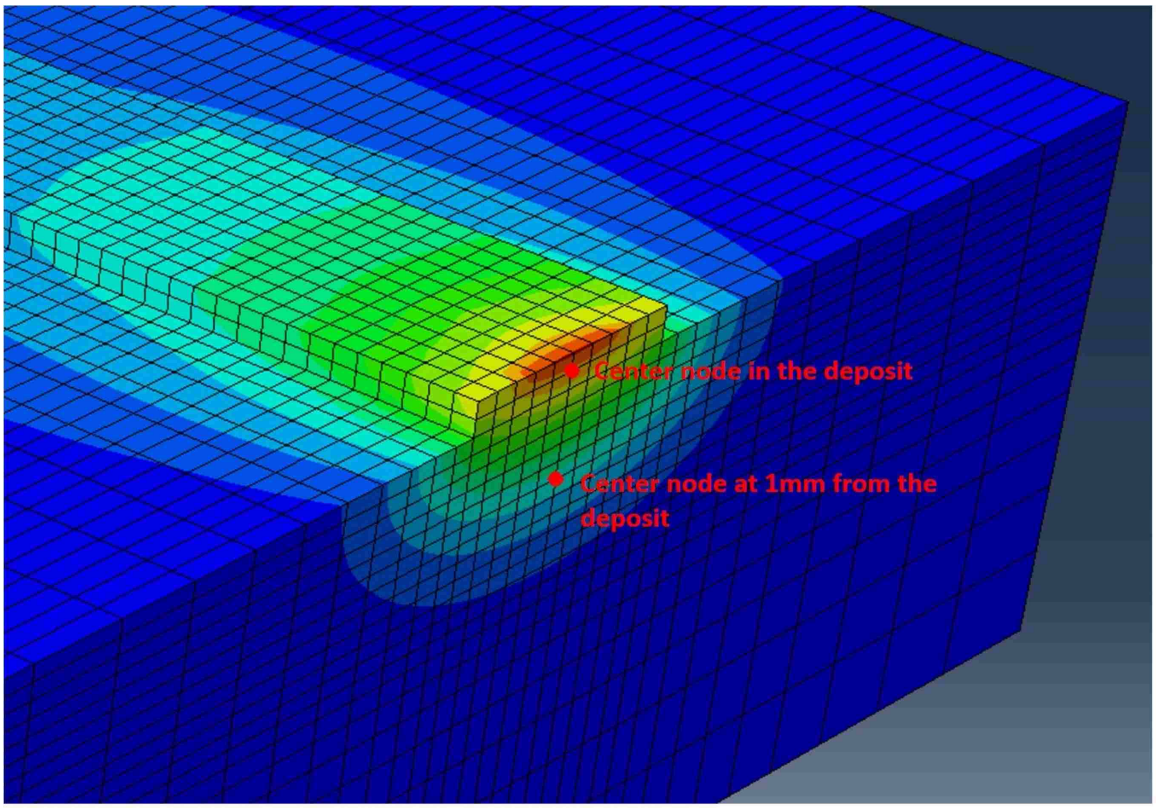

(a)

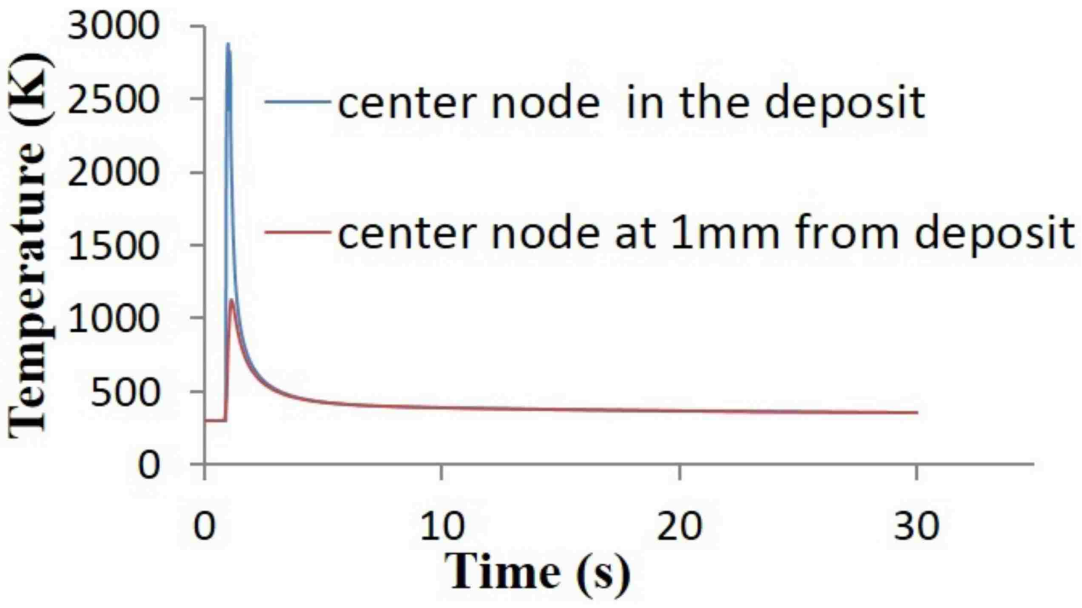

(b)

Figure 7. Temperature history at the center node in the deposit and substrate during deposition and cooling process

Table 1. Ti-6Al-4V thermal and physical properties

Temperature (K)	Thermal Conductivity ($W/(m \cdot K)$)	Density (kg/m^3)	Specific Heat ($J/(kg \cdot K)$)
300	5.9596	4419.7	547.54
500	9.1095	4388.9	590.54
700	12.2495	4358.1	633.54
900	15.3895	4327.3	676.54
1100	18.5295	4296.5	719.54
1300	20.0227	4265.7	646.83
1500	22.5627	4234.9	682.85
1700	25.1027	4204.1	718.87
1900	27.6427	4173.3	754.89
2100	37.648	3799.6	831
2300	42.448	3663.6	831
2500	47.248	3527.6	831
2700	52.048	3391.6	831
2900	56.848	3255.6	831

In order that the input of microstructure model is reliable, the temperature field is validated with four type K thermocouples. The locations are shown in Figure 8. One is located at the starting end of laser path. Another three points are located by one side of laser path. Arduino device is used to sample the temperature data. The TC position is near to the melt pool. The distance is 3-3.5mm. A laser deposition experiment is conducted with the power of 750 W, scanning speed of 600 mm/min and 2g/min for single-layer deposit. The difference between experiment and FEM modeling is less than 10 Celsius degree shown in Figure 9. In the real experiment, the substrate is fixed by the metal fixture, which resulting in the more heat conduction than the FEM model. Because of argon gas, forced convection occurred in the real experiment. This also cause lower cooling rate in the temperature simulation. Because the difference between experiment and simulation is smaller than 10%, the current FEA modeling is still considered as a reasonable simulation of temperature field, which can provide the reliable thermal input for the CA model.

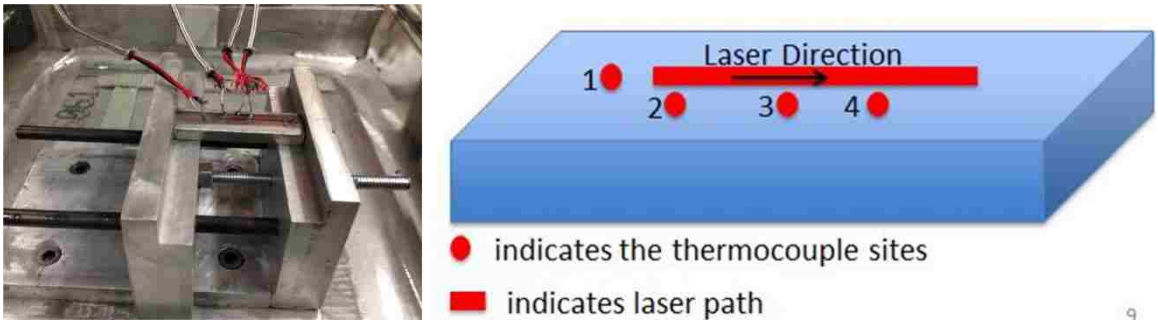

Figure 8. Thermocouples location and laser scan direction schematic diagram

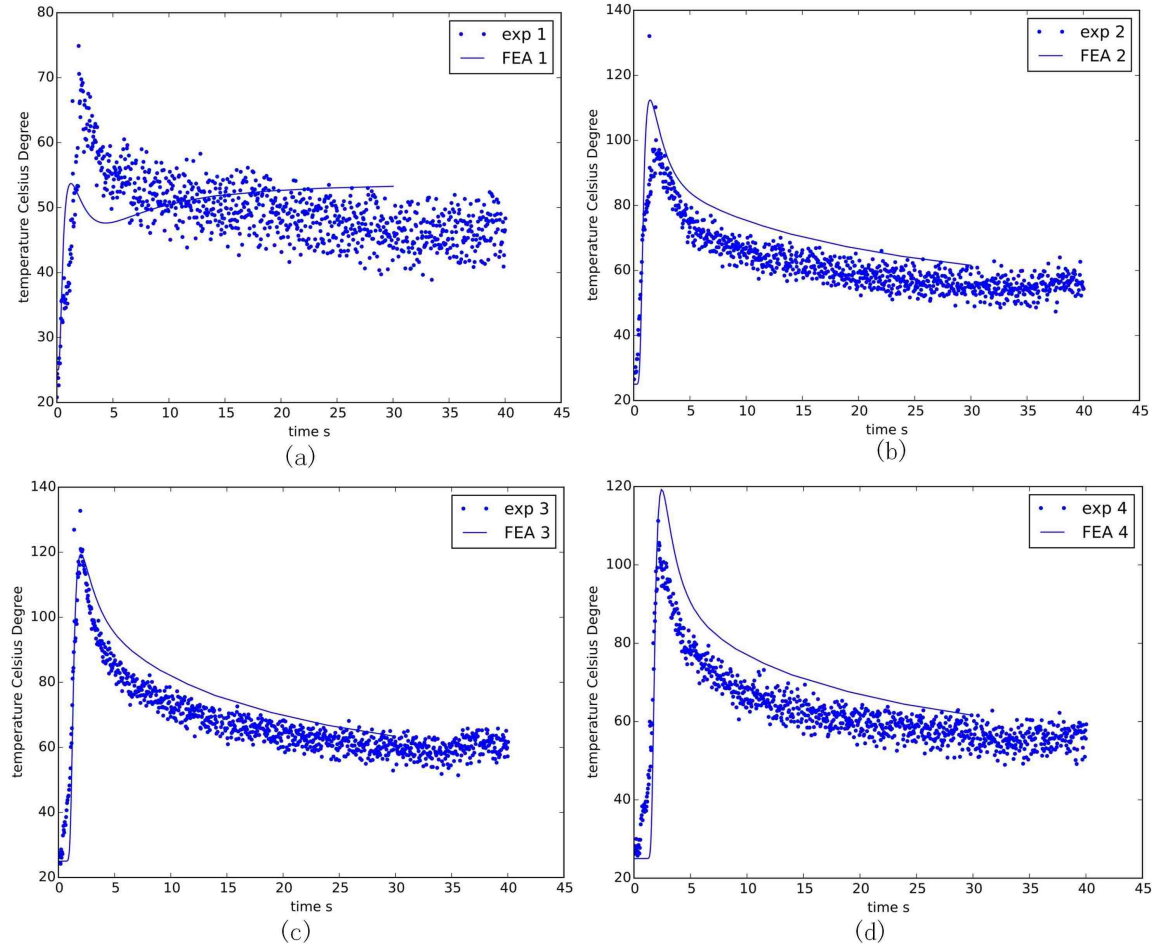

Figure 9. Temperature validation with four type K thermocouples measured at (a), (b), (c) and (d) at location 1, 2, 3, and 4, respectively

A laser deposition experiment is conducted with the power of 700 W, scanning speed of 600 mm/min and 2g/min for single-layer deposit. For this case, the cross section shown in the figure is the computational domain. The cell size for this simulation is $6\mu m \times 6\mu m$. X and Y axis represents the number of cell. The simulation result from conventional method is shown Figure 10. It can be observed that even though different grains own diverse orientation at the very beginning, the crystallographic orientation preference tend to be along the axis after several time steps. Here, different color represents various grain orientations. Finally, the equiaxed grains dominate the fusion zone. The original grain orientations are not kept during the solidification process. It doesn't agree well with the single-layer experimental result shown in Figure 12.

The developed CA grain growth method is implemented under the same condition. According to the developed CAFE simulation, the single layer simulation result is shown in Figure 11. The grain keeps its original crystallization orientation when grain growth is modelled. The columnar grain can be identified from the solid/liquid interface. When grains continue to grow towards melt pool center, some grains overgrow other grains such that there are fewer grains further away from the solid/liquid interface.

Three samples of single-layer deposits are prepared with EDM cutting, grinding, polishing and etching. The optical microscope is shown in Figure 12. The comparison between simulation and experimental results are shown in Figure 13. An average of twenty measurements per sample is performed in order to determine the average grain size number. It compares the experimental average grain size number with the predicted average grain size number. The shown data suggests that a 15% error between measurements and predictions is present. This can be considered as a reasonable prediction of grain morphology and size.

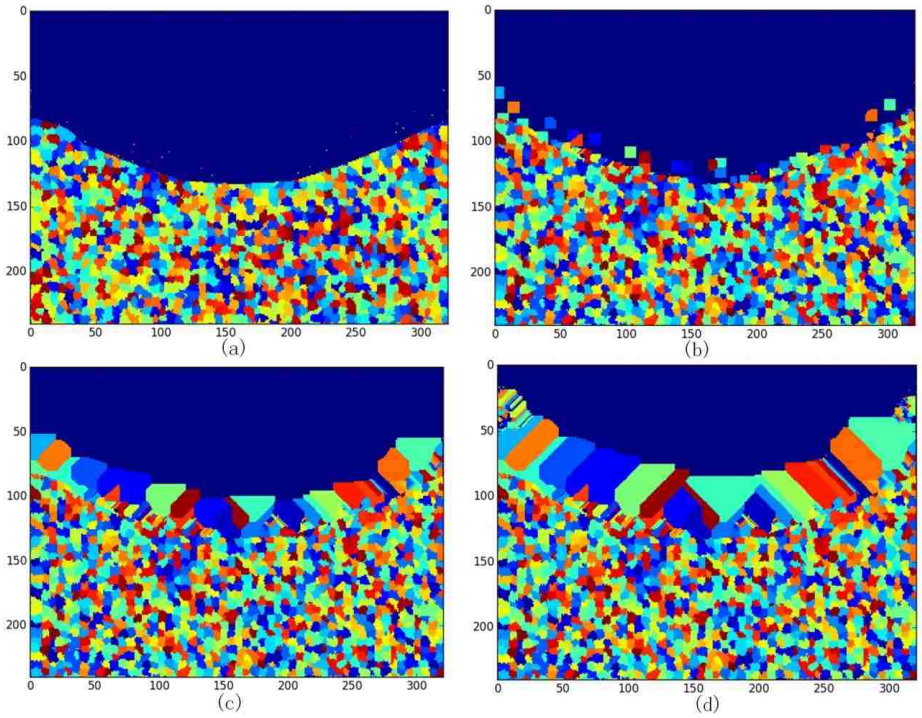

Figure 10. Grain structure of conventional growth method for single layer Ti6Al4V deposition at (a) 5ms (b) 25ms (c) 45ms (d)65ms time step

3.2. SENSITIVITY ANALYSIS

In the thermal model, the gaussian distribution heat source is simulated. The laser diameter is determined by the location of $1/e^2$ of maximum intensity. Three cases from 1.5mm to 2.5 mm are shown in Figure 14. It can be seen that the bottom temperature are the same because the input total energy are the same. The diameter difference directly influences the energy density of heat source. Therefore, the peak temperature for three cases are different. 2.5 mm temperature peak is delayed least since larger diameter makes the measured center point is affected earlier such that it arrives at the peak value earliest. For Figure 15, the power of temperature is analyzed. The combined equation is $h \approx 2.41 \times 10^{-3} \varepsilon T^{1.61}$, which power is 1.61. Power changes from 1.2 to 3. It can be observed that the valley temperature varies among different power cases. Power directly affects the combined heat transfer coefficient. When the model employs the high value of power, it

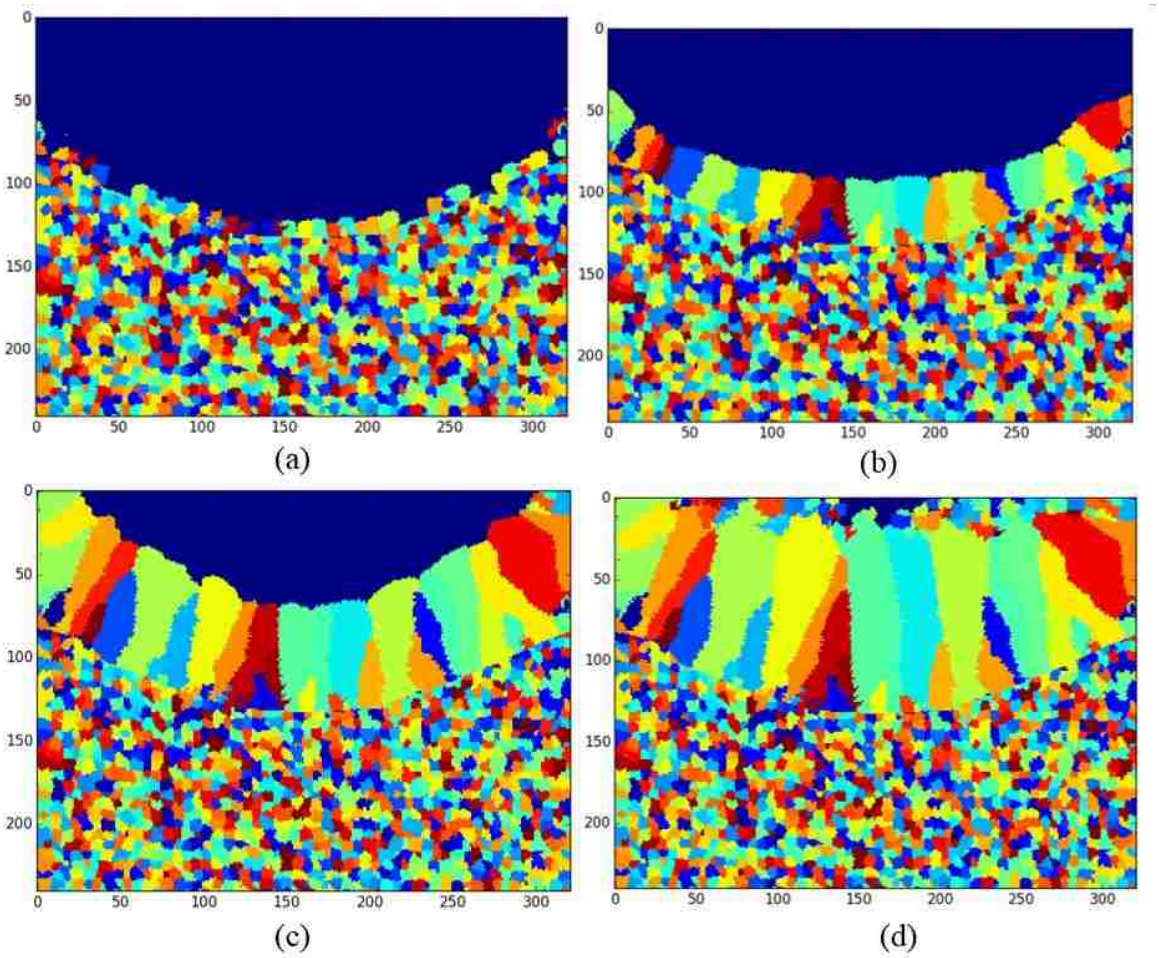

Figure 11. Grain structure of developed growth method for single layer Ti6Al4V deposition at (a) 20ms (b) 40ms (c) 60ms (d)80ms time step

Figure 12. Ti-6Al-4V single-layer deposition grain morphology at (a) 50x and (b) 200x

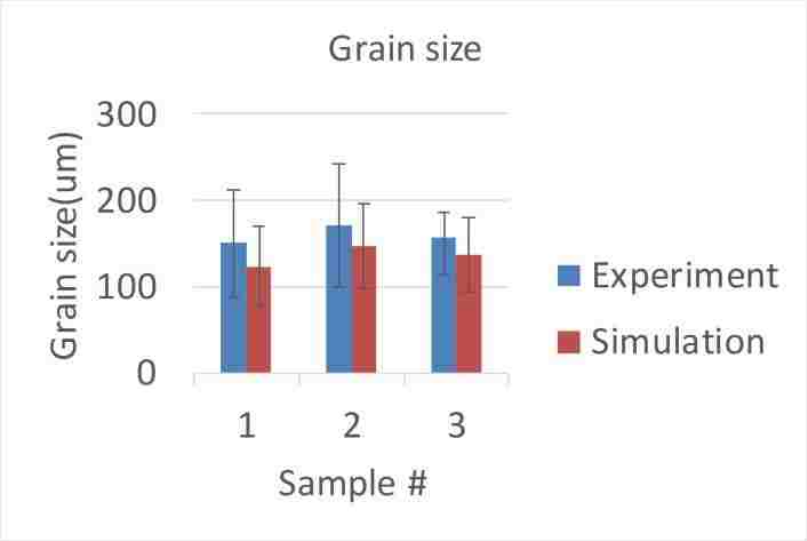

Figure 13. Grain size comparison between simulation and experiment

represents that it dissipates heat faster. Therefore, the valley temperature will be lower. However, for the peak temperature difference, it is approximately 300K, not as obvious as Figure 14. For peak temperature, heat source distribution plays a much more important role.

In the CA model, initial grain size effect on final grain morphology in the fusion zone is analyzed in Figure 16. The three grain size are $20\mu m$, $40\mu m$ and $80\mu m$. It can be seen that as the initial grain size decreases, the average grain width also decreases. In contrast to homogeneous nucleation, where every atom in the liquid is a potential nucleation site, the number of sites for heterogeneous nucleation depends on the amount and type of foreign substrate. A large initial grain size limits available nucleation sites for FZ grains. There are less nucleation occurrence at the liquid/solid interface. Competition between the grains ensures that further growth follows similar trends. Compared to electron beam welding process in the ref, the similar trend is identified.

The quantitative simulation of CET relies upon the density and activity of the heterogeneous nuclei. To illustrate the importance of the nucleation parameters (and hence grain refining), the effect of reducing the barrier to nucleation (i.e., ΔT_N) from the base

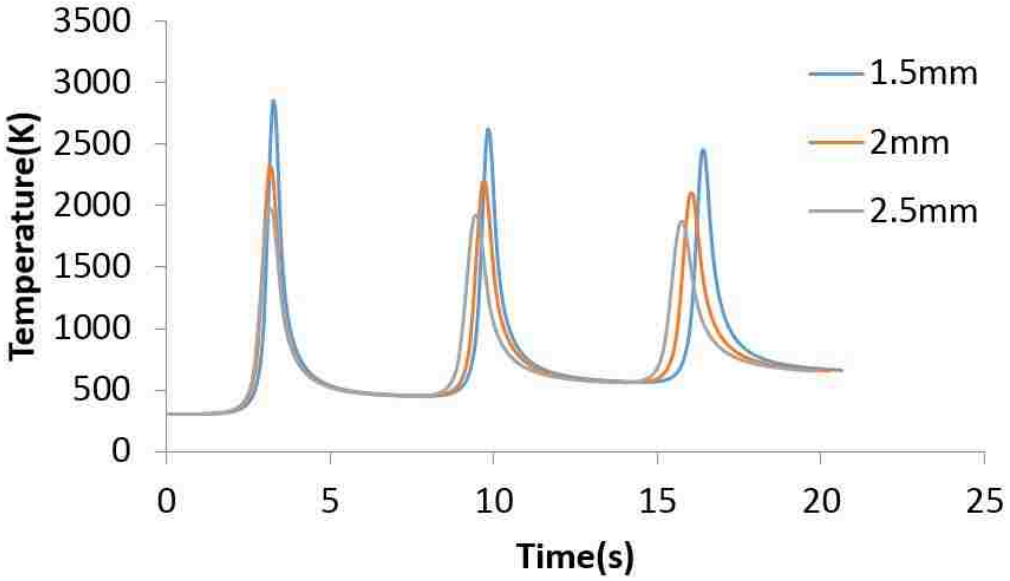

Figure 14. Laser diameter sensitivity analysis

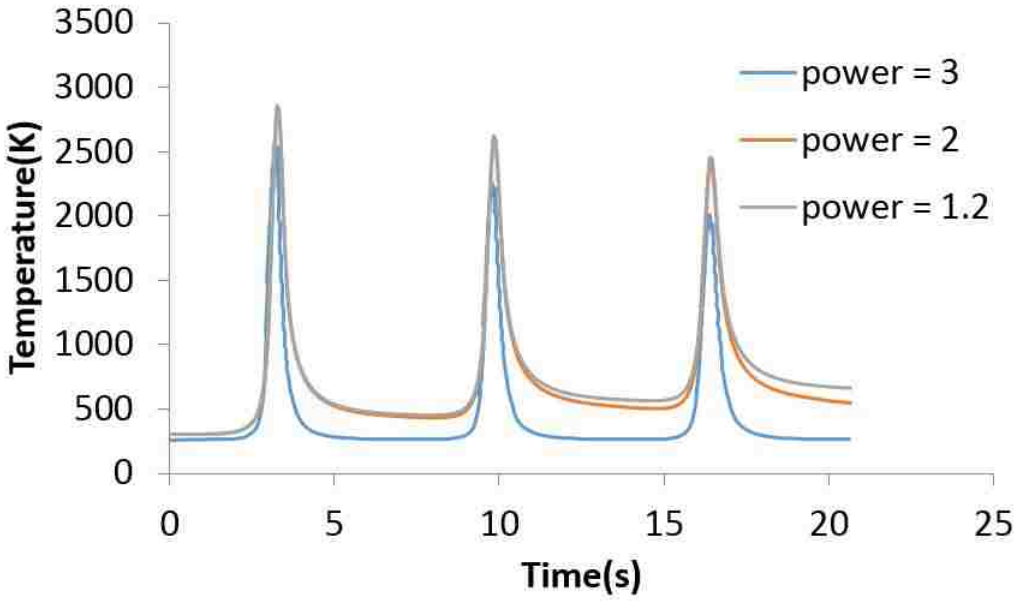

Figure 15. Temperature power sensitivity analysis

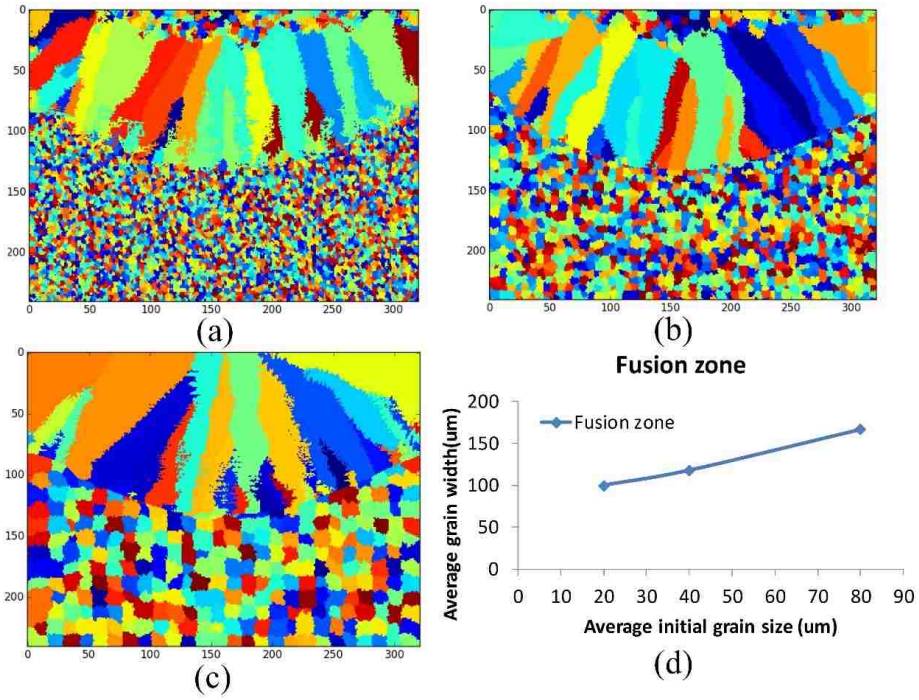

Figure 16. Initial grain size vs fusion zone grain width. (a) 20μm (b) 40μm (c) 80μm (d) relationship between initial grain size with final grain width

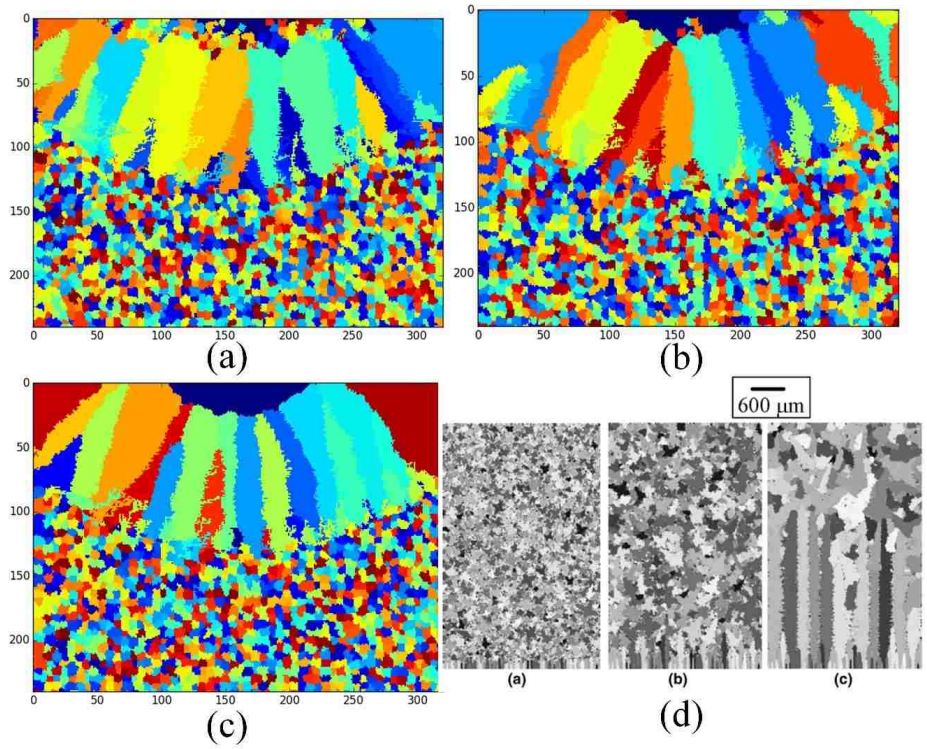

Figure 17. Mean nucleation undercooling effect on grain structure

case of ΔT_N equal to 5 K to 10 K and 20 K is shown in Figure 17. A decrease in mean nucleation undercooling favors the formation of equiaxed grains at the top. When the mean undercooling is low, there is more opportunities for nucleation in the top liquid bulk before columnar grains dominate this region.

For the columnar grains growth, the grain misorientation information is also analyzed. This is 6-layer deposit simulation from the front view. Figure 18 shows the evolution of the grain texture as a function of build height. It is clearly seen that starting from an equiaxed baseplate with no texture at low height, a strong texture develops due to grain selection with increasing build height. Within the red dashed rectangle region, the high mis-orientation becomes less in the top deposit area. But at the region close to substrate, low and high mis-orientation both exist because overgrowth of grains has not occurred at this region.

4. CONCLUSIONS

The transient temperature field of one-layer and multiple-layer deposition of Ti-6Al-4V was simulated with finite element method. The simulation result was validated by thermocouple experiment. The FE model provides the temperature at a relatively coarse scale (200) and interpolation algorithm was used to scale the temperature field to match that of the CA model. The FE-CA model predicts grain morphology evolution as the deposition cools down. Hence, the instantaneous nucleation law, grain growth, and crystallographic orientation were modeled in this study. It has been found that the developed "decentered polygon" growth method is more appropriate for the highly non-uniform temperature field, and the simulation result is more closed to the real experimental measurement compared to conventional growth method. The grain size of single layer between simulation and experiment are similar. It demonstrates that this FE-CA simulation can reasonably predict thermal history and grain morphology during this case of Direct Metal Deposition. The

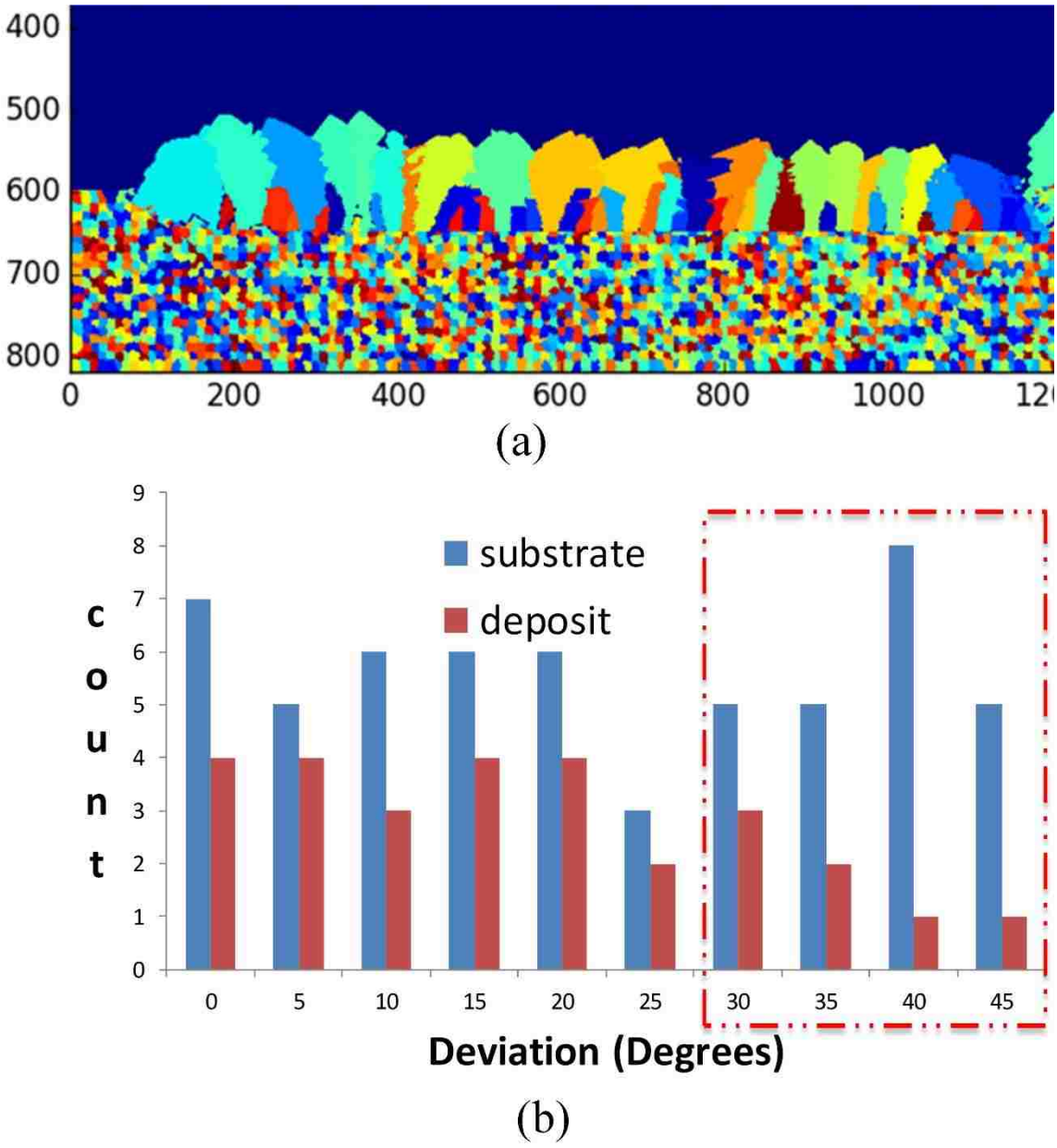

Figure 18. Deviation degrees of grains from substrate to deposit

sensitivity analysis of thermal model demonstrates the effect of laser spot diameter and temperature power effect on temperature field distribution. The initial grain size and mean undercooling effect on grain size and orientation is also quantatively analyzed.

REFERENCES

[1] Rappaz, M., 1989, "Modelling of microstructure formation in solidification processes no," 34(3).

[2] Anderson, M. ., Srolovitz, D. ., Grest, G. ., and Sahni, P. ., 1984, "Computer simulation of grain growth-I. Kinetics," Acta Metall., 32(5), pp. 783-791.

[3] Srolovitz, D. J., Anderson, M. P., Sahni, P. S., and Grest, G. S., 1984, "Computer simulation of grain growth-II. Grain size distribution, topology, and local dynamics," Acta Metall., 32(5), pp. 793-802.

[4] Saito, Y., and Enomoto, M., 1992, "Monte Carlo Simulation of Grain Growth," ISIJ Int., 32(3), pp. 267-274.

[5] Chen, L.-Q., 2002, "Phase-field models for microstructure evolution."

[6] Krill III, C. E., and Chen, L.-Q., 2002, "Computer simulation of 3-D grain growth using a phase-field model," Acta Mater., 50(12), pp. 3059-3075.

[7] B*ö*ttger, B., Eiken, J., and Steinbach, I., 2006, "Phase field simulation of equiaxed solidification in technical alloys," Acta Mater., 54(10), pp. 2697-2704.

[8] Moelans, N., Blanpain, B., and Wollants, P., 2008, "An introduction to phase-field modeling of microstructure evolution," Calphad, 32(2), pp. 268-294.

[9] Rappaz, M., and Gandin, C.-A., 1993, "Probabilistic modelling of microstructure formation in solidification processes," Acta Metall. Mater., 41(2), pp. 345-360.

[10] Gandin, C.-A., and Rappaz, M., 1994, "A coupled finite element-cellular automaton model for the prediction of dendritic grain structures in solidification processes," Acta Metall. Mater., 42(7), pp. 2233-2246.

[11] Gandin, C.-A., Desbiolles, J.-L., Rappaz, M., and Thevoz, P., 1999, "A three-dimensional cellular automation-finite element model for the prediction of solidification grain structures," Metall. Mater. Trans. A, 30(12), pp. 3153-3165.

[12] Choudhury, A., Reuther, K., Wesner, E., August, A., Nestler, B., and Rettenmayr, M., 2012, "Comparison of phase-field and cellular automaton models for dendritic solidification in Al-Cu alloy," Comput. Mater. Sci., 55, pp. 263-268.

[13] Dore, X., 2000, "Modelling of microsegregation in ternary alloys: application to the solidification of Al-Mg-Si," 48, pp. 3951-3962.

[14] Jarvis, D. J., Brown, S. G. R., and Spittle, J. A., 2000, "Modelling of non-equilibrium solidification in ternary alloys:comparison of 1D , 2D , and 3D cellular automaton finite difference simulations," 16(December), pp. 2-6.

[15] Grujicic, M., Cao, G., and Figliola, R. S., 2001, "Computer simulations of the evolution of solidification microstructure in the LENS TM rapid fabrication process," 183, pp. 43-57.

[16] Kelly, S. M., and Kampe, S. L., 2004, "Microstructural evolution in laser-deposited multilayer Ti-6Al-4V builds: Part II. Thermal modeling," Metall. Mater. Trans. A, 35(6), pp. 1869-1879.

[17] Kelly, S. M., and Kampe, S. L., "Microstructural evolution in laser-deposited multilayer Ti-6Al-4V builds: Part I. Microstructural characterization," Metall. Mater. Trans. A, 35(6), pp. 1861-1867.

[18] L*ü*tjering, G., 1998, "Influence of processing on microstructure and mechanical properties of ($\alpha + \beta$) titanium alloys," Mater. Sci. Eng. A, 243(1-2), pp. 32-45.

[19] Reddy, J. N., and Gartling, D. K., 2010, The finite element method in heat transfer and fluid dynamics, CRC PressI Llc.

[20] Phillips, L. C. A. R. L., 2005, Laser Beam Propagation through Random Media, SPIE Publications.

[21] Alimardani, M., Toyserkani, E., and Huissoon, J. P., 2007, "A 3D dynamic numerical approach for temperature and thermal stress distributions in multilayer laser solid freeform fabrication process," Opt. Lasers Eng., 45(12), pp. 1115-1130.

[22] Lampa, C., Kaplan, A. F. H., Powell, J., and Magnusson, C., 1997, "An analytical thermodynamic model of laser welding," J. Phys. D. Appl. Phys., 30(9), p. 1293.

[23] Liu, H., and Sparks, T., 2012, "Modeling and verification of temperature distribution and residual stress in laser aided metal deposition process," (1), pp. 1-7.

[24] Oldfield, W., 1966, "A quantitative approach to casting solidification: Freezing of cast iron," Trans. Am. Soc. Met., 59, p. 945.

[25] D.J.FISHER, W. K. and, 1992, "Appendix 7 and 8," Fundamentals of Solidification, TRANS TECH PUBLICATION, pp. 226-246.

[26] D.J.FISHER, W. K. and, 1992, "Appendix 9," Fundamentals of Solidification, TRANS TECH PUBLICATION, pp. 247-260.

[27] Chen, R., Xu, Q., and Liu, B., 2014, "A Modified Cellular Automaton Model for the Quantitative Prediction of Equiaxed and Columnar Dendritic Growth," J. Mater. Sci. Technol., 30(12), pp. 1311-1320.

III. MICROSTRUCTURE AND PROPERTIES OF FUNCTIONALLY GRADED MATERIALS TI6AL4V/TIC FABRICATED BY DIRECT LASER DEPOSITION

Jingwei Zhang[a], Yunlu Zhang[a], Wei Li[a], Frank Liou[a], Joseph Newkirk[b]

[a]Department of Mechanical & Aerospace Engineering

Missouri University of Science and Technology, Rolla, Missouri 65409, U.S.A.

[b]Department of Materials Science & Engineering

Missouri University of Science and Technology, Rolla, Missouri 65409, U.S.A.

ABSTRACT

Purpose:

This paper aims to manufacture Ti6Al4V/TiC Functionally Graded Material (FGM) by Direct Laser Deposition (DLD) using Ti6Al4V and TiC powder. The objective is to investigate the effect of process parameters and TiC composition on microstructure, Vickers hardness and mechanical properties.

Design/methodology/approach:

Powder blends with three different volume percentages of Ti6Al4V and TiC were used as feed material for DLD process. Five experiments with different values of laser power and scan speed were conducted to investigate the effect on microstructure and Vickers hardness for different compositions of feed material. Mini-tensile tests were performed to evaluate the mechanical properties of the FGM samples. Digital Image Correlation (DIC) was applied to estimate Young's modulus and ultimate tensile stress (UTS) of heterogeneous material.

Findings:

This paper indicates that primary carbide, eutectic carbide and un-melted carbide phases are formed in the FGM deposit. As the energy density was increased, the primary and secondary dendrite arm spacing was found to increase. As TiC composition was increased, Young's modulus increased and UTS decreased. The dendritic morphology of primary TiC growth was expected to cause low resistance for crack propagation causing lower UTS values. Tensile specimens cut in vertical orientation were observed to possess higher values of Young's modulus in comparison with specimens cut horizontally at low carbon content.

Originality/value:

Current work presents unique and original contributions from the study of miniature FGM tensile specimens using DIC method. It investigates the effect of specimen orientation and TiC content on Young's modulus and UTS. The relationship between energy density and dendritic arm spacing was evaluated. The relationship between laser power and scan speed with microstructure and Vickers hardness was investigated.

Keywords: Direct Metal Deposition, Functionally Graded Material, Microstructure, Mechanical Properties, Ti6Al4V/TiC

1. INTRODUCTION

Titanium alloys, especially the Ti6Al4V alloy, are widely used in the aerospace, medical and manufacturing industries. Ti6Al4V possesses excellent properties, such as high strength-to-weight ratio, high temperature strength, low density and excellent corrosion resistance [1][2]. However, Ti6Al4V doesnâĂŹt have high surface hardness, stiffness or wear resistance. This limits the use of Ti6Al4V in applications involving extreme conditions. Metal Matrix Composites (MMC) with ceramic reinforcements are often considered as candidate materials for applications requiring improved mechanical, tribological and material properties. TiC can be deposited together with Ti6Al4V since it has the low den-

sity, similar coefficient of thermal expansion, high hardness, and high YoungâĂŹs modulus [3][4][5]. This system can be developed to improve microstructure and increase structural stiffness and hardness in the aerospace and medical field.[6] Liu et al.[7] investigated TiC/TA15 composite for microstructure and room temperature tensile properties. Material fabricated with different TiC volume fractions ranging from 5% to 15% were tested during Laser Melting Deposition (LMD) process. It was found that the failure mechanism of the composites during tensile test was significantly influenced by particle cracking. Candel et al. [8] concluded that material and tribological properties were significantly improved by the incorporation of TiC particles to reinforce hot rolled Ti6Al4V. Liu et al.[9] studied tensile strength and elongation of LMD fabricated TiC/TA15 composite with 10% TiC reinforcement at elevated temperature. Ochonogor et al. [10] developed titanium metal matrix composite to improve the hardness and wear resistant properties by changing TiC content. Mahamood et al. [11] studied the effect of transverse speed on microstructure, microhardness and wear resistance of laser deposited Ti6Al4V/TiC composite.

However, when the TiC content is increased, deposit becomes prone to crack initiation and high porosity. This is due to the obvious differences in coefficient of thermal expansion, ductility and toughness of Ti6Al4V and TiC [12][13]. FGMs can be selected as a candidate material to improve material properties and fabricate crack and pore free deposited parts. Liu and DuPont [12] developed functionally graded TiC/commercially pure Ti materials by Laser Engineered Net Shaping (LENS) with compositions ranging from pure titanium to approximately 95 vol% TiC. Microstructural characteristics, micro-hardness, and phase formation of different composition were investigated. The macro-crack can be observed in the homogeneous deposits. Wang et al. [14] investigated the compositionally graded building of Ti6Al4V reinforced with TiC material under fixed laser power and scan speed by direct laser fabrication. Properties of microstructure and tribology were also studied. Obielodan and Stucker [15] investigated the effect of different dual-material transition joint designs on tensile and flexural strength for Ti6Al4V/5wt%TiC and Ti6Al4V/10wt%TiC

Table 1. Process parameters on previous research

Ref.	Power (W)	Scan speed (mm/min)	TiC size (μm)	Ti6Al4V size (μm)	Powder feed rate (g/min)	Beam size (mm)
6	750	600	32-45	45-75	0.3-2.2	1
7	3200	900-6300	<60	150-200	2.88	2
8	420	510	45-150	45-150	-	0.5-1
9	1500-1800	240	75-150	75-150	-	3
10	1100	150	100-200	wire	-	3
11	200-270	changing	45-150	125-210	changing	2

composite. Mechanical properties of the joint structures, including flexural strength, tensile strength, yield strength and elastic modulus were evaluated. Mahamood and Akinlabi [16] developed functionally graded Ti6A4V/TiC composite by comparing deposit dimension, microstructure and wear resistance under fixed and optimized process parameters. All the process parameters and powder size of previous work are listed in Table 1.

Although some research has been performed on this FGM system, there is very few knowledge on the influence of laser power and scan speed on microstructure, hardness, and mechanical properties. The composition effect on Young's modulus and UTS is also rarely investigated. In the current work, microstructure, hardness and X-ray diffraction were performed on DLD fabricated Ti6Al4V/TiC FGM. Influence of laser power and scan speed variation on material properties are discussed. In order to improve the stiffness of Ti6Al4V structure, the optimized laser power is employed to build Ti6Al4V/TiC FGM deposit. The mechanical properties for different compositions and specimen orientations in an FGM are investigated. Miniature tensile tests were conducted, and DIC analysis was implemented for estimation of mechanical properties in horizontal and vertical directions. The fracture mechanism for different TiC compositions was also analyzed. The experiment result can combine both material advantages and provide the data for future high stiffness structure selection.

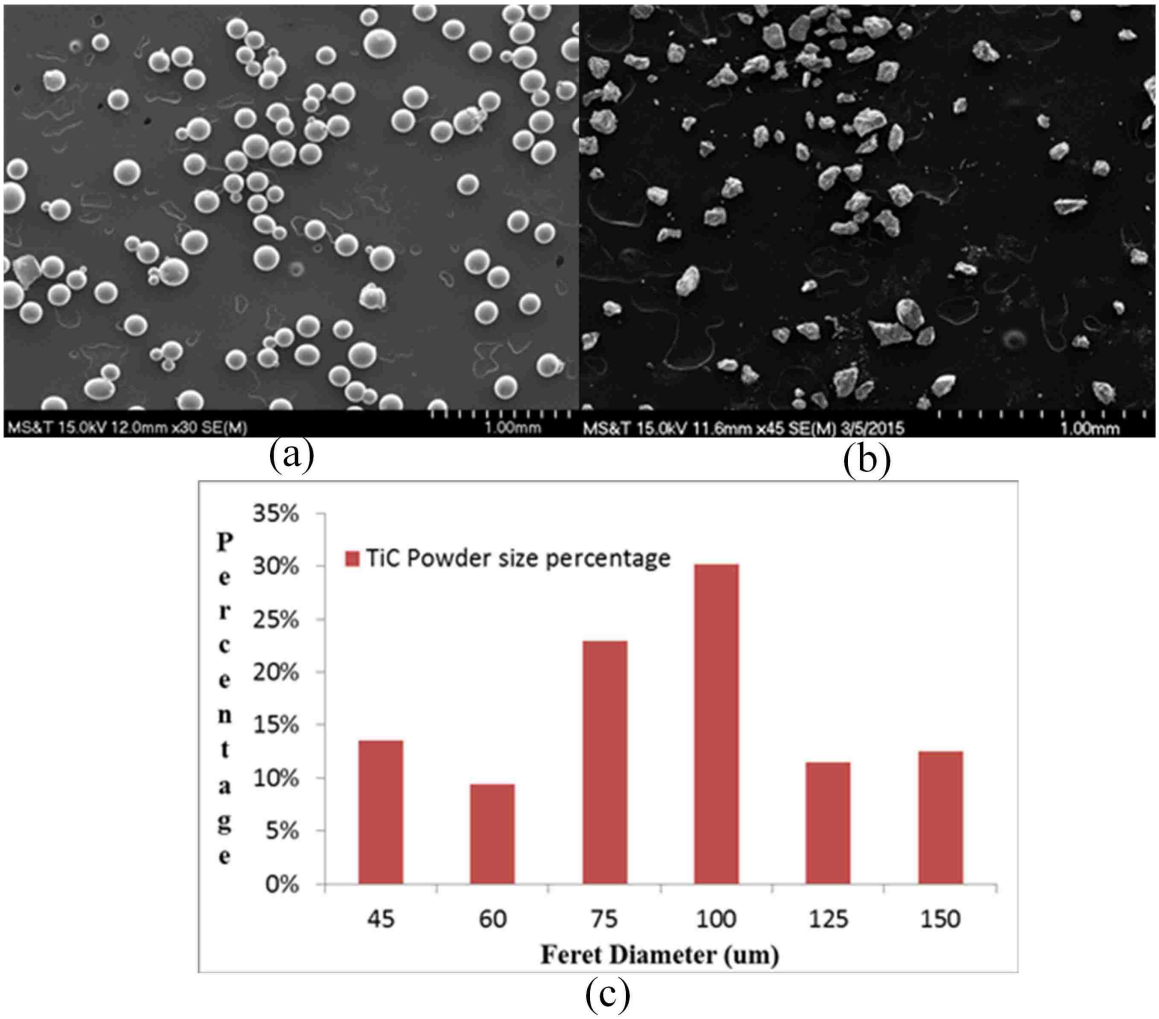

Figure 1. SEM images of (a) gas atomized spherical Ti6Al4V powder and (b) irregular TiC powder. (c) TiC powder sieve analysis data

2. EXPERIMENTAL PROCEDURES

The feed material used in this study was gas atomized Ti6Al4V powder mixed with varied volume percentages of TiC powder. The particle sizes of the Ti6Al4V spherical powder was between $125\mu m$and $250\mu m$. TiC powder (99.5% pure) had particle size distribution of $45\mu m$ to $150\mu m$, which is similar to chosen powder size ($45\mu m$ – $200\mu m$) in Ref [10] - [15]. TiC particles have been sieved to remove the fine particle ($< 45\mu m$) and large particle ($> 150\mu m$). The particle size distribution is shown in Figure 1(c). The

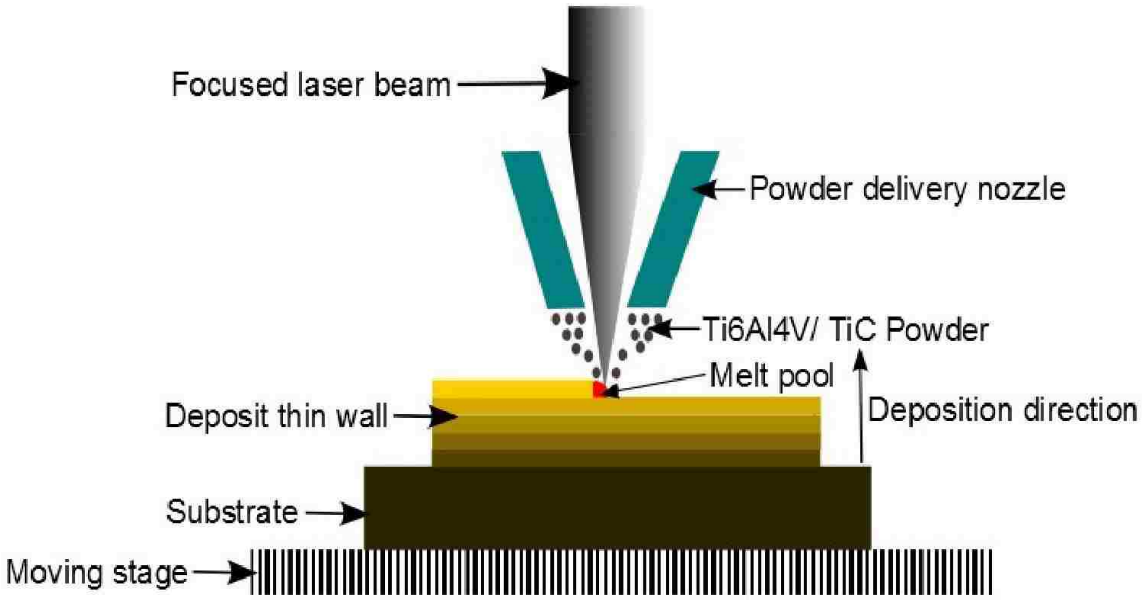

Figure 2. Schematic layout of the DLD system performing thin-wall deposition

substrate material was grade 5 hot rolled Ti6Al4V alloy. Powder blends of TiC and Ti6Al4V with 10vol%, 20vol% and 30vol% TiC were premixed for manufacturing the TiC/Ti6Al4V FGM parts. TiC powder was not gas atomized and was hence irregular. However, the blended powder was expected to flow freely due to the spherical Ti6Al4V. The experiments were carried out using a 1kW Nd-YAG laser (IPG), edge nozzle powder delivery system and a computer controlled multiple axes translator.

The two powders (Ti6Al4V and TiC powder) were dried in a furnace for 20 minutes at 180 C, then mixed for 30 minutes on a TURBULA mixer. The laser beam diameter was approximately 2mm. Argon gas was utilized to shield the deposition and transport mixed powder. The surface of the substrate was ground with SiC abrasive paper and then degreased with alcohol prior to the DLD process. This was done to remove oxide scale and impurities from the surface of the deposit. A schematic diagram of the laser deposition process is shown in Figure 2.

Table 2. Experimental parameters

Sample No.	Power (W)	Scan speed (mm/min)	Substrate size	Energy density (J/mm^2)	Composition (volume %)
Sample 1	400	300	2”× 0.5”× 0.25”	40.0	10%-20%-30%
Sample 2	550	200	2”× 0.5”× 0.25”	82.5	10%-20%-30%
Sample 3	550	300	2”× 0.5”× 0.25”	55.0	10%-20%-30%
Sample 4	550	400	2”× 0.5”× 0.25”	41.3	10%-20%-30%
Sample 5	700	300	2”× 0.5”× 0.25”	70.0	10%-20%-30%

Substrate material was cut to 2 inch by 0.5 inch by 0.25 inch size. Laser power ranged from 400W to 700W, and the scan speed varied from 200mm/min to 400mm/min. Therefore, the energy density varied from was 40.0 to 82.5 J/mm^2. The experimental parameters are shown in Table 2. Specimens were cut, ground, polished and etched in order to do for microscope observation and material property testing. A FEI Helios NanoLab DualBeam SEM was used to observe the cross sectional microstructure. A DURAMIN tester was utilized to measure the Vickers hardness. A Philips MRD was used to do XRD analysis on the deposit. An INSTRON UTM was used to conduct miniature tensile test. Ti6Al4V and TiC powder morphology is shown in Figure 1.

$$Energydensity = \frac{P}{v \times w} \tag{1}$$

P is laser power, v is scanning speed and w is the diameter of laser spot.

Another set of experiments was conducted to fabricate and test the mechanical properties of FGM specimens with different TiC composition and changing process parameters. The thin-wall FGM structures were deposited with 10vol% to 30vol% TiC. Each composition was deposited for 60 layers. To ensure good bonding with the substrate, initial three

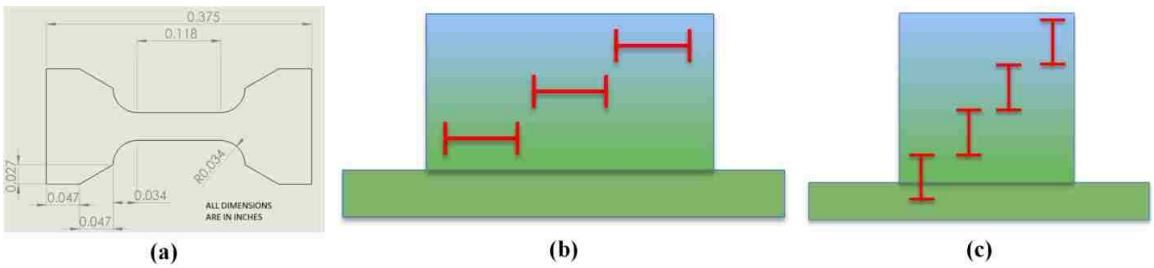

Figure 3. Mini-tensile illustration of (a) Specimen size (b) horizontal and (c) vertical specimen layout illustration

layers were performed at a power of 800W higher than the appropriate optimal power levels. Then laser power drops to 450W gradually and keeps at 450W in order to prevent too much heat input and keep constant melt pool width and depth. The powder feed rate is constantly $3g/min$. The laser beam diameter was maintained at approximately $2mm$ at a focal distance of $750mm$ to the substrate. The layer thickness is set approximately at $0.2mm$. The scan speed was set constant to $550mm/min$ for all the thin-wall depositions. The dimension of as-deposited sample is shown in Figure 4. Mini tensile specimens [17] , were prepared with EDM, dimensions of the specimen are shown in Figure 3(a). Mini tensile specimens were cut in horizontal and vertical patterns, schematic layout of the specimen location is shown in Figure 3(b) and (c). Direct measurement of elongation using an extensometer is difficult owing to the small size of the specimen. Therefore, DIC analysis [18][19] was employed to calculate displacement, principal and secondary strain and Young's modulus. It is appropriate for heterogeneous materials as it provides a distribution rather than a single measurement. During the mini tensile test, constant crosshead speed of $0.045mm/min$ was maintained. The composition of TiC was limited to 30% as significant flaws were noticed at higher content.

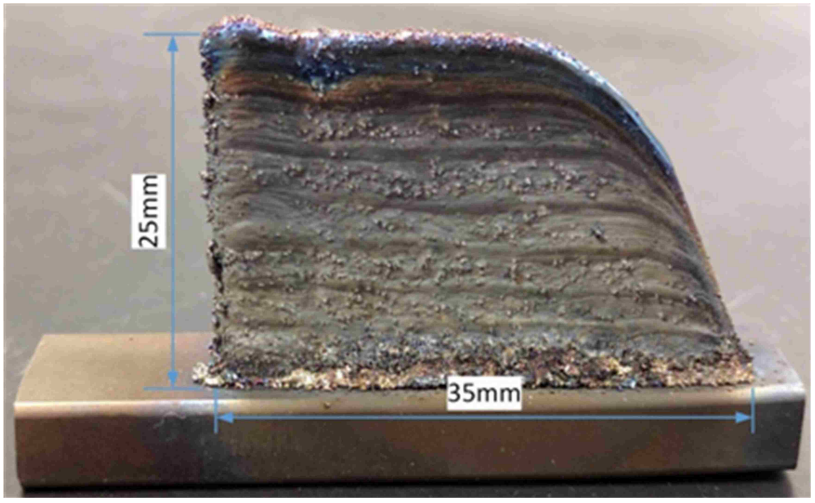

Figure 4. Photograph showing dimension of FGM sample

3. RESULTS AND DISCUSSION

3.1. MICROSTRUCTURE

Figure 5 shows the SEM images of microstructure taken from Ti-6Al-4V/TiC FGM along the substrate to the top of the deposit. The images show a variation in microstructure as TiC content was increased. The material was etched using Kroll's reagent. The shape and size of TiC are significantly different from the fed TiC powder, suggesting melting of the powder. Both dissolution and solidification of TiC were observed. Based on the Ti-C binary phase diagram [20], the eutectic temperature is about 1670 degree Celcius and TiC will form as the primary phase at a carbon atomic content of 2% and larger. For 10 vol% TiC mixed powder, the carbon atomic percentage is approximately 8%, which is higher than the eutectic point. When the carbon concentration in the remaining liquid phase decreases to the eutectic point, the TiC + β binary eutectic reaction occurs. When the cooling rate is high, nonequilibrium cooling causes pseudo eutectic reaction to occur near eutectic point, which forms eutectic carbide as shown in Figure 5(b) and Figure 5(c) [21]. In Figure 5(d), both primary carbide and eutectic carbide appear in the microstructure. When carbon percentage is increased, the hypereutectic reaction occurs before the temperature drops to

eutectic temperature. As carbon content increases, the difference between the liquidus temperature and eutectic temperature becomes larger, which allows more time for primary carbide growth. Therefore, the long primary dendritic carbide can be seen in Figure 5(e). At the top of the deposit, some un-melted particles of carbides were found to remain. This presence was attributed to insufficient heat input caused by the increasing TiC content.

Figure 6 shows the morphology of primary and eutectic carbide under different energy densities. It can be observed that, as energy density was increased from 40 J/mm^2 to 70 J/mm^2, the size of primary carbide becomes larger. The primary dendrite arm spacing (PDAS) from material made under three different energy densities are $19.0 \pm 1.2\mu m$, $26.1 \pm 5.7\mu m$ and $61.9 \pm 15.7\mu m$. The average secondary dendrite arm spacing (SDAS) of three different laser power is $1.2 \pm 0.2\mu m$, $1.7 \pm 0.2\mu m$ and $2.9 \pm 0.5\mu m$. The PDAS and SDAS increase due to the higher laser power resulting in a slower cooling rate during solidification. This provides dendrites with more time to develop and grow.

3.2. HARDNESS RESULTS

The deposited samples were tested with Vickers hardness at 1 kg force and 10 second loading time. Figure 7 shows the indentation positions on one of the FGM samples. The Vickers hardness profile is shown in Figure 8 and Figure 9. The lowest hardness value appears in Ti-6Al-4V substrate region, which is 300 HV1. Along the deposition direction, the hardness value increases to approximately 600 HV1 owing to the increasing content of carbide. The nonlinear increase might be due to the diffusion of carbon and the difference between unmelted carbide and re-solidified carbide hardness. The Vickers hardness measurement found, three laser power and scan speed doesn't significantly influence FGM deposit hardness distribution.

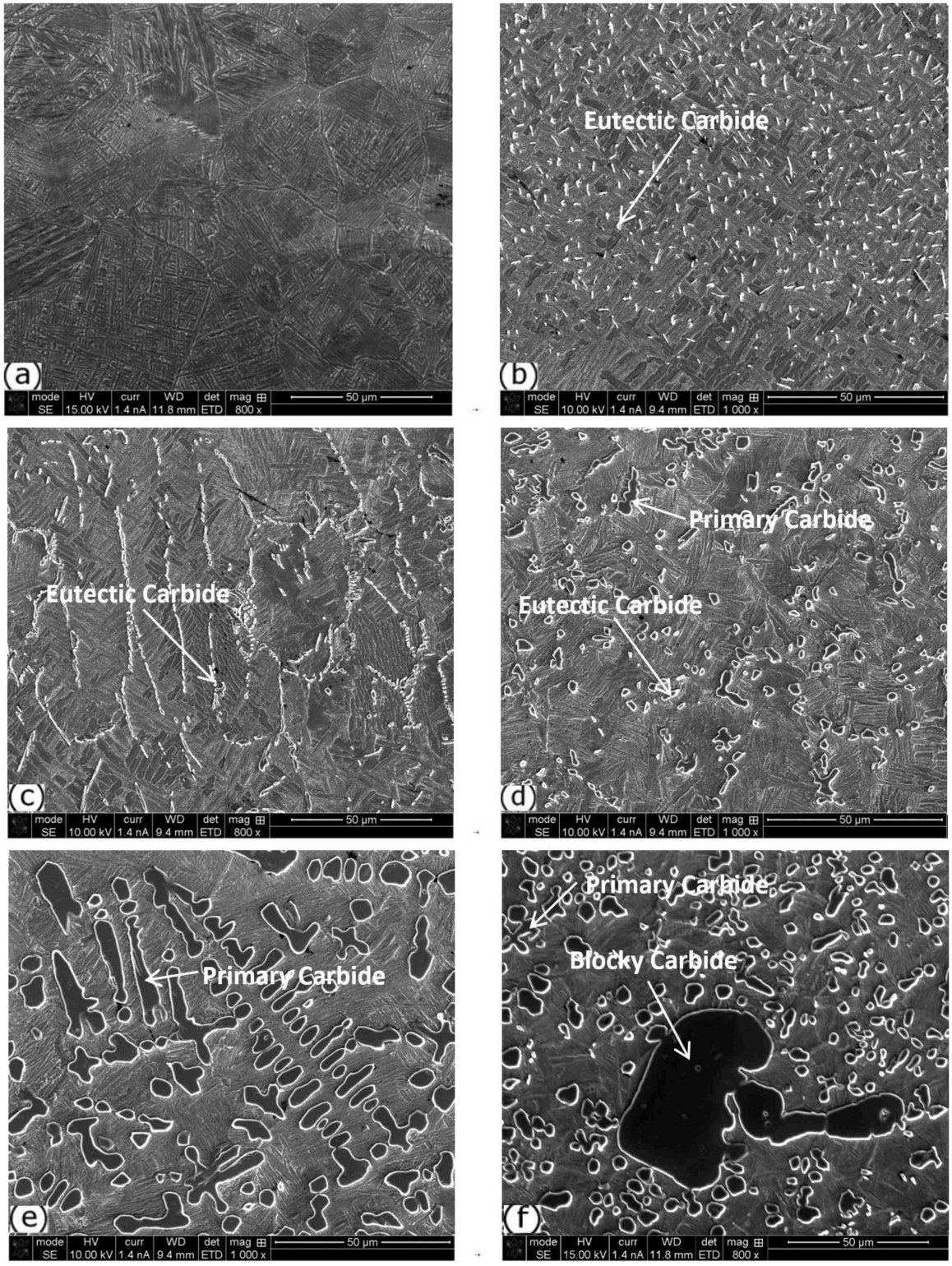

Figure 5. Microstructure of Ti-6Al-4V/TiC FGM deposit: (a)-(f): SEM images of microstructure along the height of the FGM deposit.(a, b): 0-10% TiC; (c, d): 10%-20% TiC; (e, f): 20%-30% TiC

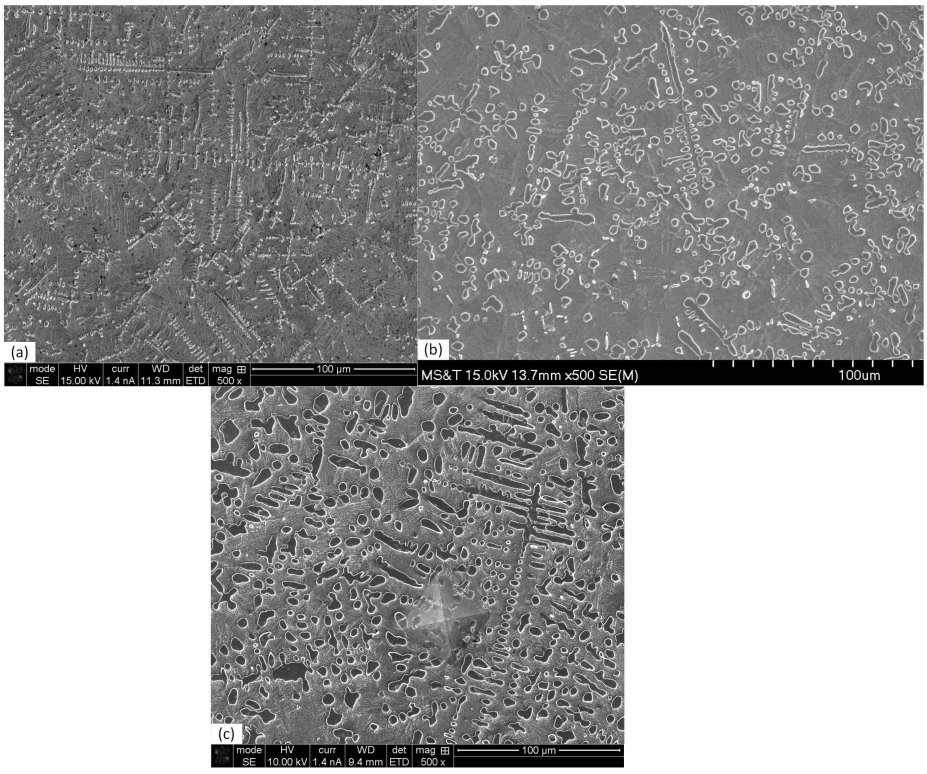

Figure 6. Microstructure of re-solidified carbide made under different energy density: (a) $40.0J/mm^2$ (400W, $300mm/min$). (b) $55.0J/mm^2$ (550W, $300mm/min$). (c) $70.0J/mm^2$ (700W, $300mm/min$)

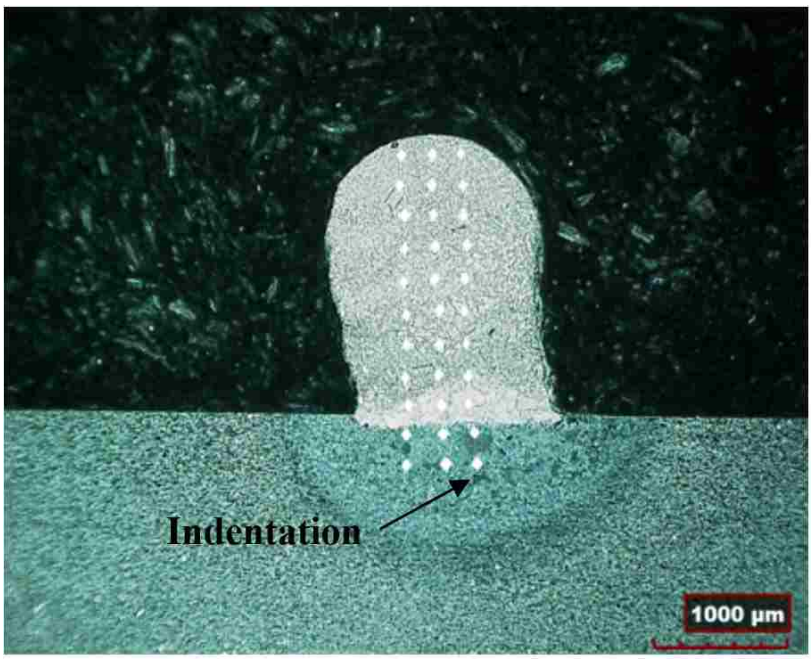

Figure 7. Optical dark field image showing Vickers hardness measurements performed across the height of the FGM

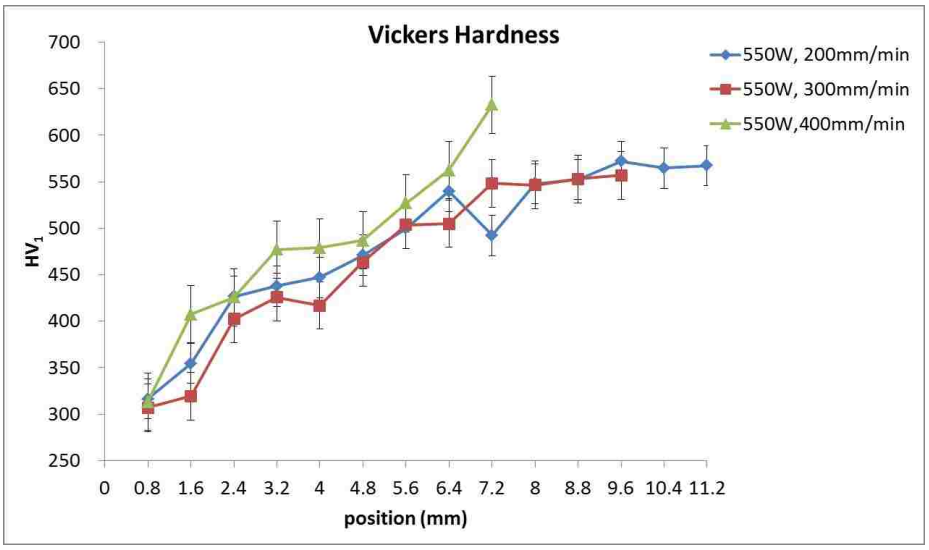

Figure 8. Vickers hardness distribution from substrate to top deposit for different scan speeds

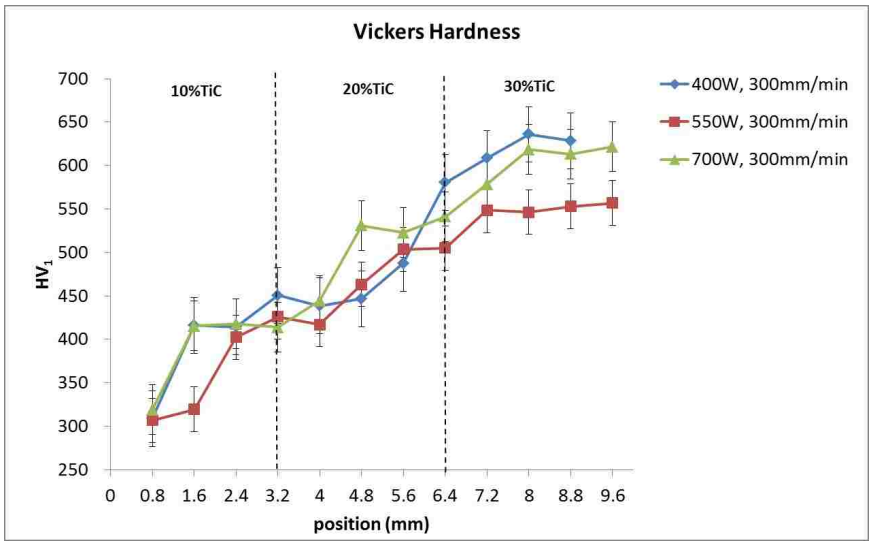

Figure 9. Vickers hardness distribution along the FGM (with approximate TiC composition variation markers) with different laser power

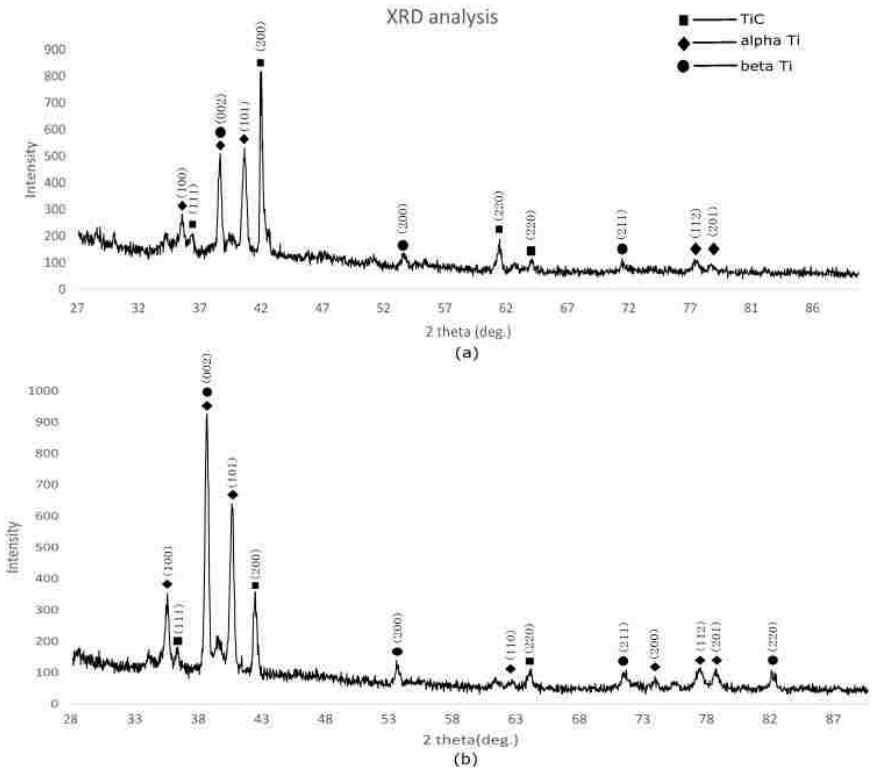

Figure 10. XRD peak patterns taken from: (a) top of the FGM and (b) bottom of the FGM

3.3. XRD ANALYSIS

Figure 10 shows X-Ray Diffraction (XRD) patterns taken from different locations along the height of the deposit. XRD was able to detect α-Ti (HCP), β-Ti (BCC) and TiC (FCC) phases. An approximate area of $2mm \times 2mm$ was analyzed in the XRD measurement. There were no intermetallic phases identified in the analyzed area. At the top of Ti-6Al-4V/TiC deposit, the TiC phase was dominant over α-Ti and β-Ti, this is in agreement with the microstructure and hardness result. Although α-Ti content was higher than β-Ti, there was β-Ti still remaining. This can be attributed to the high cooling rate in the solidification process. At the bottom of Ti6Al4V/TiC deposit, α-Ti and β-Ti were the dominant phases.

3.4. MECHANICAL PROPERTIES

Figure 11 indicates the first principal strain field estimates on a horizontal specimen taken from 30%TiC section of the FGM. X and Y axes represent the pixel locations along two directions. The images show uniform elongation at different instances during the test. This demonstrates that there is no significant compositional variation within the Region Of Interest (ROI). It can be seen that the DIC analysis is suitable to obtaining the whole strain field during the whole tensile process. Because of the small dimension of mini-tensile specimens, the extensometer cannot be fixed on the specimen directly. The slippery displacement between the specimen and extensometer will result in the error of strain measurement. DIC method, based on the feature match between different images, can eliminate the extensometer limitation. Figure 12 indicates the stress-strain curves gathered from testing different TiC composition specimens cut in vertical and horizontal orientation. The starting values for strain are different among the specimens due to the differences in elongation from preload (100N). The variation of initial strain results from the differences in Young's Modulus. The 10vol% TiC, specimen's stress-strain curve indicates yielding. However 20% and 30% TiC specimens do not indicate clear yielding. It can therefore be said that, the ductility declines significantly as the TiC content is increased. Figure 13 indicates that the stiffness increases with the percentage of TiC. Young's modulus of as-DLDed Ti6Al4V is approximately 95 GPa [22]. For FGM samples, Young's modulus increases from 108 ± 8GPa to 167 ± 17GPa. For 10% and 20% TiC specimens, Young's modulus from vertical specimens is slightly higher than horizontal specimens. This difference is expected due to the preferential solidification occurring during thin-wall fabrication. These thin-wall structures are expected to have vertical columnar grains due to the high vertical thermal gradient. The higher modulus of high carbon content is due to the existence of eutectic, primary and unmelted carbide under high cooling rate. It can be observed that the UTS drops with the increase of TiC content as shown in Figure 14. UTS values decline from 991 ± 56MPa for 10vol% TiC to 551 ± 34MPa for 30% TiC. The influence of horizontal

and vertical layout was observed to be insignificant. This strength drop can be attributed to two reasons: the lower damage tolerance of the composite and the premature failure of TiC particle. Although carbon in the solid solution would result in the strength increase to some extent [23], this is only valid when carbon percentage is smaller than a critical value. The solubility of carbon in Ti matrix is significantly low based on the Ti-C binary phase diagram [24]. When carbon content is much higher than the solid solubility under high cooling rate, the remaining carbon cannot be solved in the matrix. The premature failure of TiC particles results in crack initiation and propagation during the tension, thus decreasing the strength of the composites. The large blocky carbide particles with defects are readily vulnerable to the premature fracture, thus inducing the high multi-axis stress. Moreover, high carbon content degrades the ductility of the composite and inhibits the matrix plastic flow, which makes the composite more sensitive to initial defects at a low stress level.

SEM images of the fracture surfaces from mini-tensile specimens are shown in Figure 15. Acronym meanings are shown here, PF: particle fracture. SC: secondary cracking. PPH: particle pullout hole. The fracture surface of Ti6Al4V is shown in Figure 15(a). This dimpled surface represents ductile fracture. Figure 15(b), (c) and (d) show the brittle fracture surfaces on the tensile samples. It can be stated that, cracks generated in the primary titanium carbide readily propagate along the dendritic carbide phase. Some particle fracture (PF) and secondary cracking (SC) can also be observed on the fracture surfaces. From Figure 15(c) and (d), the smooth cleavage planes of TiC can be clearly seen. Most un-melted TiC particles are expected to be broken directly and particle fracture can be clearly observed. The dendritic shapes on the fracture surface indicate fractures around the dendritically solidified TiC. TiC is also expected to dissolve into titanium matrix before until the maximum solid solubility of carbon is achieved, making the matrix brittle. These brittle fracture show the adverse effect of excess TiC on strength and ductility [25]. Some degree TiC clustering was observed on the fracture surface, this was similar to observations in previous work[26]. This clustering is expected to reduce the ductility due to TiC fracture

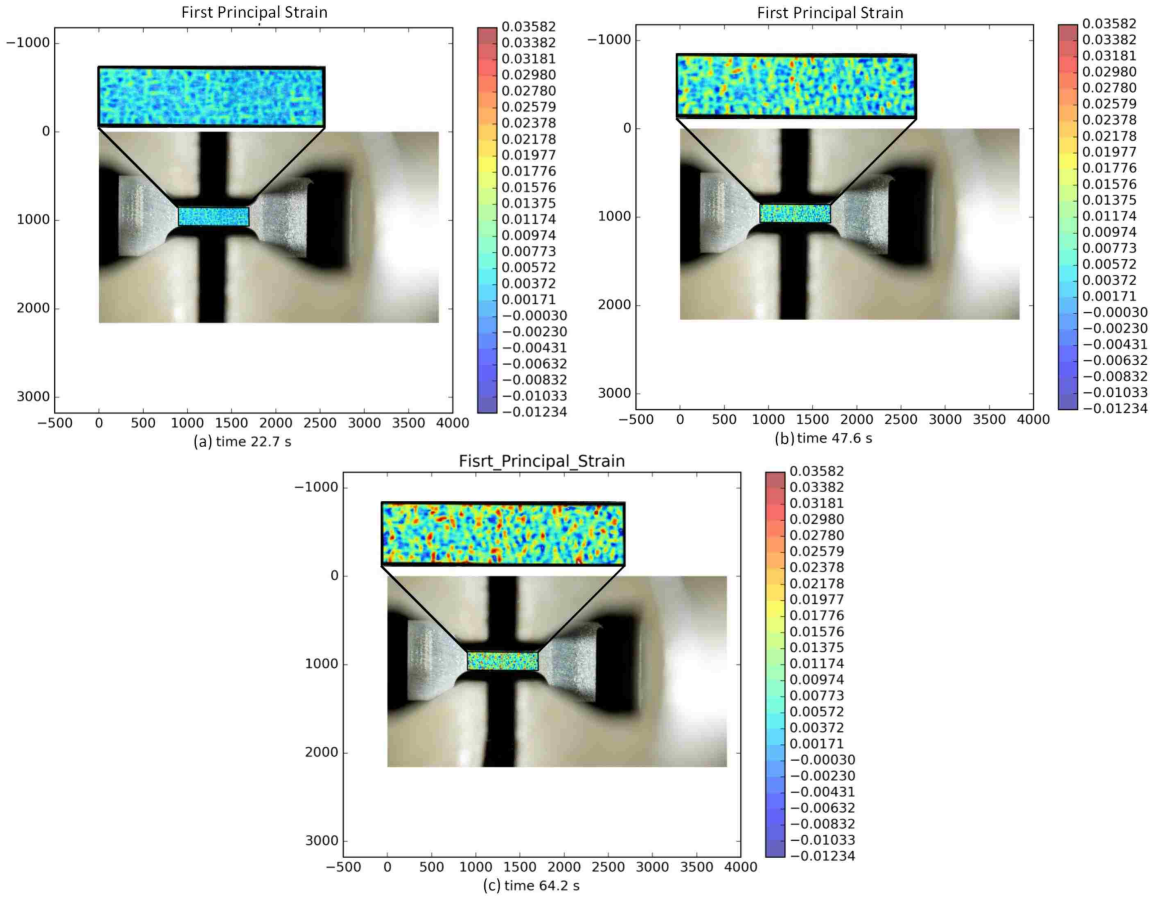

Figure 11. First principal strain field of 30% TiC horizontal specimen at (a) time = 22.7s (b) time = 47.6s and (c) time = 64.2s during mini-tensile test

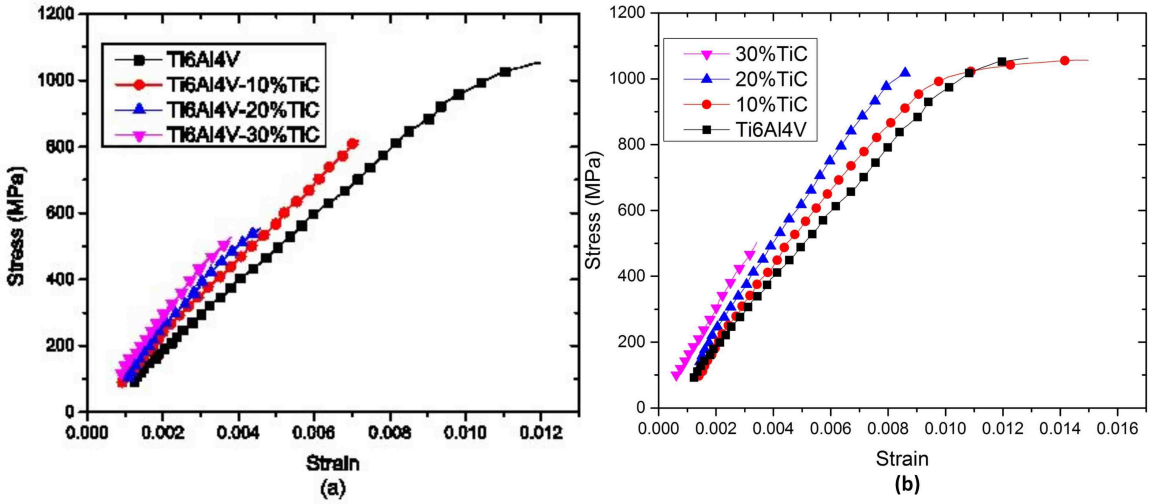

Figure 12. Mini-tensile stress-strain curves for Ti6Al4V, 10%TiC, 20%TiC and 30% TiC with (a) horizontal and (b) vertical specimens

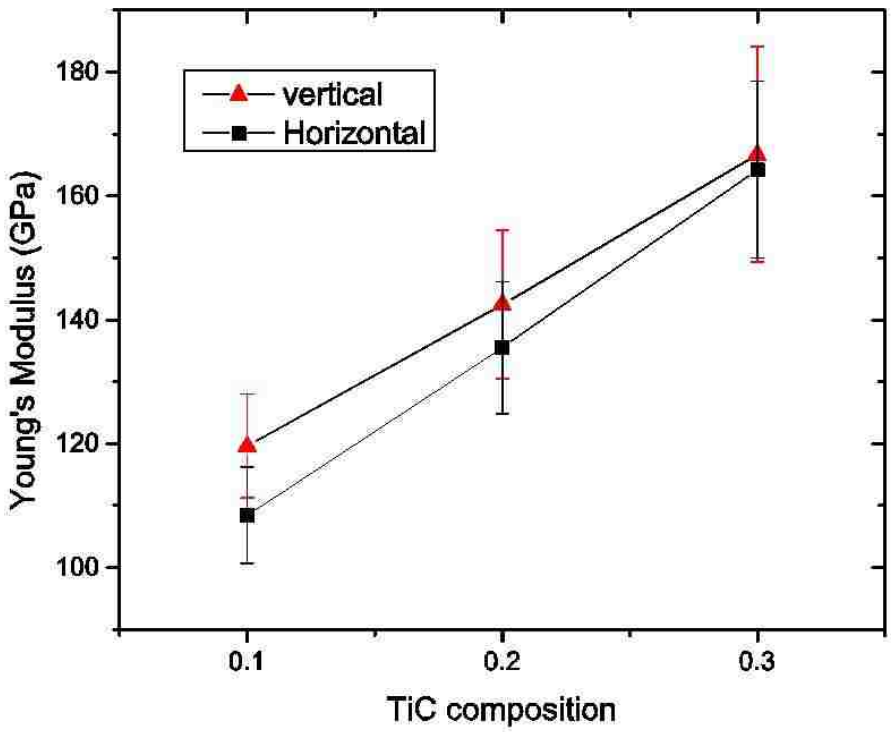

Figure 13. Young's modulus for different TiC composition with horizontal and vertical specimens

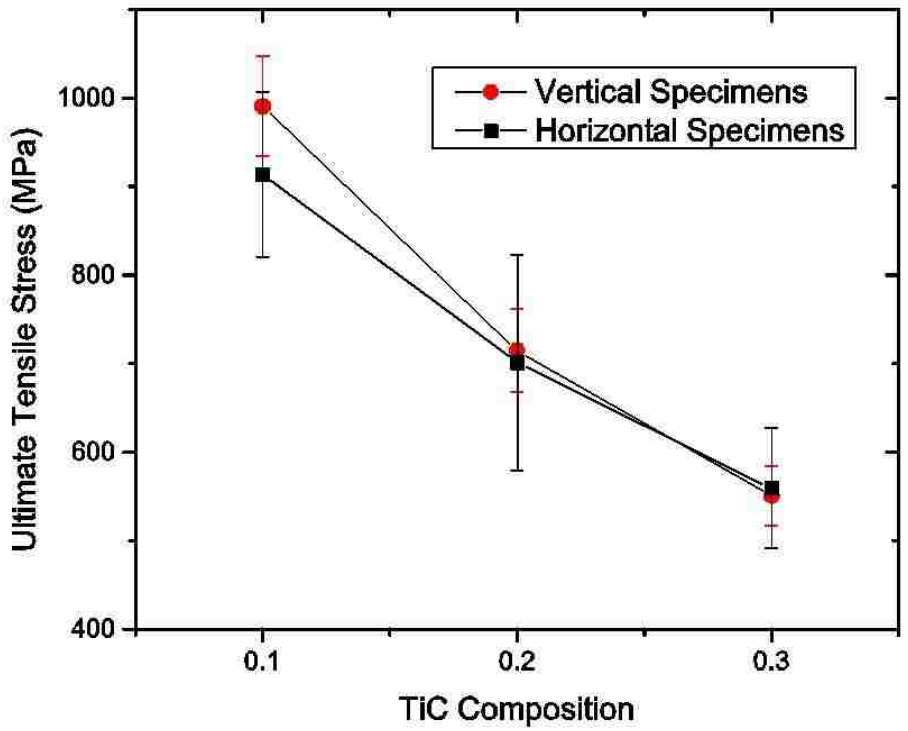

Figure 14. UTS for different TiC composition with horizontal and vertical specimens

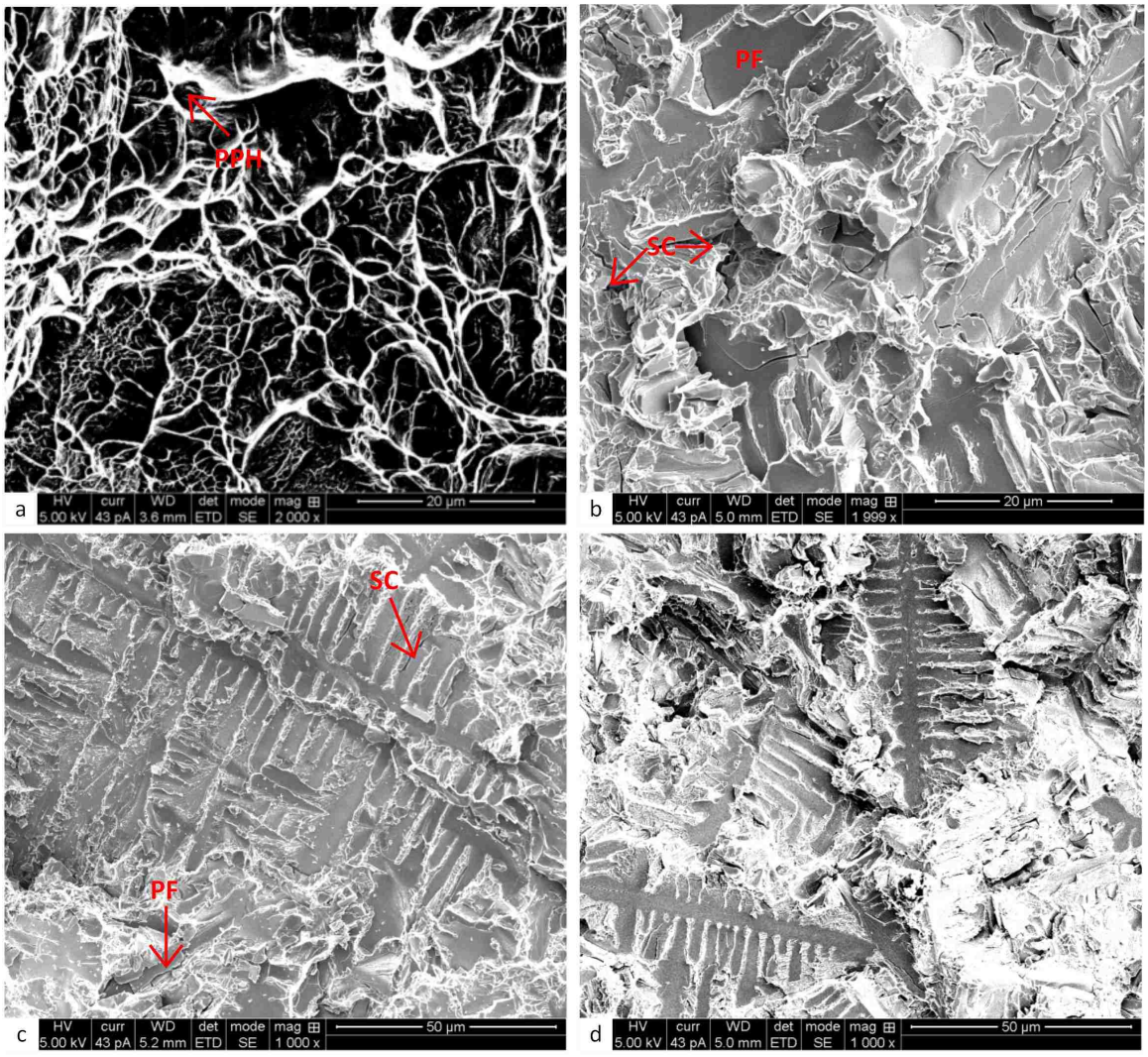

Figure 15. SEM micrographs of tensile fracture surface indicating (a) ductile fracture in Ti6Al4V and (b) (c) (d) brittle fracture with micro-cracks in 10%, 20% and 30% TiC

and plastic instability at low strain [27][28][29]. Micro-cracks have also been found on the fracture surfaces. The existence of these micro-cracks decreases the resistance against crack propagation in the matrix. Uneven distribution of TiC un-melted particles was observed in the 30%vol. section of the FGM. This can increase the possibility of failure substantially [30].

4. CONCLUSIONS

1) Ti-6Al-4V/TiC FGM from 0 vol% to 30 vol% was successfully fabricated by DLD process using premixed powder as the feed material. Primary carbide, eutectic carbide and un-melted carbide phases were observed in the microstructure. α-Ti, β-Ti and FCC structure of TiC were detected by XRD.

2) As energy density was increased, the primary and secondary dendrite arm spacing size also observed to increases.

3) The Vickers hardness measurements revealed an increase from 300VH1 to 600VH1 from along the height of the FGM. Among the chosen set of processing parameters no significant differences in hardness were produced.

4) DIC analysis was found appropriate for investigating mechanical properties of heterogeneous mini-tensile specimens. Measurements of Young's modulus from vertical specimens were slightly higher than those of horizontal specimens. Young's modulus increases and UTS decreases with increasing TiC content. Young's modulus varies from $108 \pm 8GPa$ to $164 \pm 14GPa$, the UTS drops from $991 \pm 56MPa$ for 10vol% TiC to $551 \pm 34MPa$ for 30% TiC.

REFERENCES

[1] Alcisto, J., Enriquez, A., Garcia, H., Hinkson, S., Steelman, T., Silverman, E., Valdovino, P., Gigerenzer, H., Foyos, J., Ogren, J., Dorey, J., Karg, K., McDonald, T., and Es-Said, O. S., 2011, "Tensile Properties and Microstructures of Laser-Formed Ti-6Al-4V," J. Mater. Eng. Perform., 20(2), pp. 203-212.

[2] Brandl, E., Baufeld, B., Leyens, C., and Gault, R., 2010, "Additive manufactured Ti-6Al-4V using welding wire: comparison of laser and arc beam deposition and evaluation with respect to aerospace material specifications," Phys. Procedia, 5, pp. 595-606.

[3] Zhu, J. H., Liaw, P. K., Corum, J. M., and McCoy, H. E., 1999, "High-temperature mechanical behavior of Ti-6Al-4V alloy and TiC p /Ti-6Al-4V composite," Metall. Mater. Trans. A, 30(6), pp. 1569-1578.

[4] Kim, Y.-J., Chung, H., and Kang, S.-J. L., 2002, "Processing and mechanical properties of Ti6Al4V\ TiC in situ composite fabricated by gasâĂŞsolid reaction," Mater. Sci. Eng. A, 333(1-2), pp. 343-350.

[5] Stanley Abkowitz, Susan M. Abkowitz, Harvey Fisher, P. J. S., 2004, "CermeTi discontinuously reinforced Ti-matrix composites: Manufacturing, properties, and applications," J. Miner. Met. Mater. Soc., 56(5), p. 37.

[6] HuÂÍbler, R., 1999, "Hardness and corrosion protection enhancement behaviour of surgical implant surfaces treated with ceramic thin films," Surface & Coatings Technol., pp. 1111-1115.

[7] Liu, D., Zhang, S. Q., Li, A., and Wang, H. M., 2009, "Microstructure and tensile properties of laser melting deposited TiC/TA15 titanium matrix composites," J. Alloys Compd., 485(1-2), pp. 156-162.

[8] Candel, J. J., AmigÃş, V., Ramos, J. A., and Busquets, D., 2010, "Sliding wear resistance of TiCp reinforced titanium composite coating produced by laser cladding," Surf. Coatings Technol., 204(20), pp. 3161-3166.

[9] Liu, D., Zhang, S. Q., Li, A., and Wang, H. M., 2010, "High temperature mechanical properties of a laser melting deposited TiC/TA15 titanium matrix composite," J. Alloys Compd., 496(1-2), pp. 189-195.

[10] Ochonogor, O. F., Meacock, C., Abdulwahab, M., Pityana, S., and Popoola, A. P. I., 2012, "Effects of Ti and TiC ceramic powder on laser-cladded Ti-6Al-4V in situ intermetallic composite," Appl. Surf. Sci., 263(0), pp. 591-596.

[11] Mahamood, R. M., Akinlabi, E. T., Shukla, M., and Pityana, S., 2013, "Scanning velocity influence on microstructure, microhardness and wear resistance performance of laser deposited Ti6Al4V/TiC composite," Mater. Des., 50(0), pp. 656-666.

[12] Liu, W., and DuPont, J. N., 2003, "Fabrication of functionally graded TiC/Ti composites by Laser Engineered Net Shaping," Scr. Mater., 48(9), pp. 1337-1342.

[13] Zhang, Y., Wei, Z., Shi, L., and Xi, M., 2008, "Characterization of laser powder deposited Ti-TiC composites and functional gradient materials," J. Mater. Process. Technol., 206(1-3), pp. 438-444.

[14] Wang, F., Mei, J., and Wu, X., 2007, "Compositionally graded Ti6Al4V + TiC made by direct laser fabrication using powder and wire," Mater. Des., 28(7), pp. 2040-2046.

[15] Obielodan, J., and Stucker, B., 2013, "Characterization of LENS-fabricated Ti6Al4V and Ti6Al4V/TiC dual-material transition joints," Int. J. Adv. Manuf. Technol., 66(9-12), pp. 2053-2061.

[16] Mahamood, R. M., and Akinlabi, E. T., 2015, "Laser metal deposition of functionally graded Ti6Al4V/TiC," Mater. Des., 84, pp. 402-410.

[17] S. Karnati, I. Axelsen, F. F. Liou, J. W. N., 2016, "Investigation of tensile properties of bulk and slm fabricated 304l stainless steel using various gage length specimens," solid freedom fabrication, p. 13.

[18] Verhulp, E., Rietbergen, B. va., and Huiskes, R., 2004, "A three dimensional digital image correlation technique for strain measurements in microstructures," J. Biomech., 37(9), pp. 1313-1320.

[19] Kang, J., Ososkov, Y., Embury, J. D., and Wilkinson, D. S., 2007, "Digital image correlation studies for microscopic strain distribution and damage in dual phase steels," Scr. Mater., 56(11), pp. 999-1002.

[20] Predel, B., 2012, “C - Ti (Carbon - Titanium) BT - B - Ba âĂę Cu - Zr: Supplement to Subvolumes IV/5B, IV/5C and IV/5D,” B. Predel, ed., Springer Berlin Heidelberg, Berlin, Heidelberg, pp. 147-149.

[21] Liya Regel, W. R. W., 2000, Processing by Centrifugation, Kluwer Academic Publishers-Plenum Publishers, New York.

[22] Wang, F., Mei, J., Jiang, H., and Wu, X., 2007, “Laser fabrication of Ti6Al4V/TiC composites using simultaneous powder and wire feed,” Mater. Sci. Eng. A, 445-446, pp. 461-466.

[23] Jaffee, R. I., 1958, “The physical metallurgy of titanium alloys,” Prog. Met. Phys., 7, pp. 65-163.

[24] J. L. Murray, T. B. Massalski, L. L. B. and H. B., 1986, Binary alloy phase diagrams, Metals Park.

[25] de Castro, V., Leguey, T., Monge, M. A., MuÃśoz, A., Pareja, R., and Victoria, M., 2002, “Discontinuously reinforced titanium matrix composites for fusion applications,” J. Nucl. Mater., 307-311, P, pp. 691-695.

[26] da Silva, A. A. M., dos Santos, J. F., and Strohaecker, T. R., 2005, “Microstructural and mechanical characterisation of a Ti6Al4V/TiC/10p composite processed by the BE-CHIP method,” Compos. Sci. Technol., 65(11-12), pp. 1749-1755.

[27] Segurado, J., Gonz*á*lez, C., and LLorca, J., 2003, “A numerical investigation of the effect of particle clustering on the mechanical properties of composites,” Acta Mater., 51(8), pp. 2355-2369.

[28] Poza, P., and Llorca, J., 1996, “Fracture toughness and fracture mechanisms of Al-Al_2O_3 composites at cryogenic and elevated temperatures,” Mater. Sci. Eng. A, 206(2), pp. 183-193.

[29] Hong, S.-J., Kim, H.-M., Huh, D., Suryanarayana, C., and Chun, B. S., 2003, "Effect of clustering on the mechanical properties of SiC particulate-reinforced aluminum alloy 2024 metal matrix composites," Mater. Sci. Eng. A, 347(1-2), pp. 198-204.

[30] Choe, H., Abkowitz, S., Abkowitz, S. M., and Dunand, D. C., 2008, "Mechanical properties of Ti-W alloys reinforced with TiC particles," Mater. Sci. Eng. A, 485(1-2), pp. 703-710.

SECTION

2. SUMMARY AND CONCLUSIONS

Since prediction, and control of microstructure and mechanical properties are critical to meeting strict industrial requirement, it has attracted a lot of attention during conventional metal manufacturing process, such as casting, under different conditions. However, there is few investigations focused on microstructure simulation and mechanical properties under different process parameters during DMD process. It is challenging because the whole process, compared to the traditional manufacturing process, is a non-equilibrium, multi-phase change, multi-component, and highly non-uniform field phenomena.

A multi-scaled predictive model is developed to simulate grain structure evolution during the DMD process. The transient temperature field of one-layer and multiple-layer deposition of Ti-6Al-4V is simulated with macro-scale finite element method. The FE model provides the temperature at a relatively coarse scale and linear interpolation algorithm was used to scale the temperature field to match that of the CA model. The FE-CA model can predict grain morphology evolution as the cycling heating and cooling occurs. Hence, the instantaneous nucleation law, grain growth rate, and crystallographic orientation selection are modeled in this study. It has been found that columnar grains dominate in the multiple-layer deposition in the simulation. The grain size becomes larger when the position is closer to the top area of the deposition because of grain overgrowth among columnar grains, which matches well with the optical microscopic result. It demonstrates that this FE-CA simulation can reasonably predict thermal history and grain morphology during DMD.

In order to simulate grain structure evolution under highly non-uniform temperature field, a “decentered polygon” grain growth method is developed in the CA model. It can simulate heterogeneous nucleation sites, grain growth orientation selection and growth

rate, epitaxial growth of new grains on the interface, remelting of preexisting grains, metal addition, grain competitive growth, and columnar to equiaxed transition phenomenon within substrate and melt pool domain. Compared to the previous grain growth method, it has been proved that the simulation result, modeling overgrowth and keeping crystallographic orientation, is more closed to the real experimental measurement. The grain size of single layer and multiple layer between simulation and experiment are similar.

In order to investigate the effect of process parameters and composition on microstructure and mechanical properties during DMD, crack-free Ti-6Al-4V/TiC FGM from 0 vol% to 30 vol% is successfully fabricated by premixed powder as the feed material. Primary carbide, eutectic carbide and un-melted carbide phases are observed in the microstructure. α-Ti, β-Ti and FCC structure of TiC are detected by XRD. As energy density is increased, the primary and secondary dendrite arm spacing size also observed to increases. The Vickers hardness measurements revealed an increase from 300VH1 to 600VH1 from along the height of the FGM. Among the chosen set of processing parameters, no significant differences in hardness were produced. Digital image correlation analysis is found appropriate for investigating mechanical properties of heterogeneous mini-tensile specimens. Measurements of Young's modulus from vertical specimens were slightly higher than those of horizontal specimens. Young's modulus increases and UTS decreases with increasing TiC content. Young's modulus varies from $108 \pm 8GPa$ to $164 \pm 14GPa$, the UTS drops from $991 \pm 56MPa$ for 10vol% TiC to $551 \pm 34MPa$.

The overall outcomes of this dissertation addressed several key issues which challenge the application of direct metal deposition. It develops a multi-scale model to simulate grain structure evolution during deposition process. The new grain growth method is developed so that it is more appropriate for high cooling rate and non-uniform field condition. It also analyzes the effect of composition and process parameters on as-deposit part's microstructure and properties during DMD process.

VITA

Jingwei Zhang was born in Zhangjiakou city, Hebei province, China. He received his Bachelor of Science degree in Mechanical Engineering in July 2011 from Shanghai Maritime University, Shanghai City, China. In May 2018, he received his Doctor of Philosophy in Mechanical Engineering from Missouri University of Science and Technology, Rolla, Missouri, USA. His research interests included microstructure simulation, heat transfer simulation, additive manufacturing, functionally graded material. During his Ph.D. study, he authored and co-authored five journal papers, and four conference papers.